# Fabrication of Fiber Bragg Gratings with A Direct-Write Method

Damon Marco Colpo

Spring 2024

# Acknowledgement

I would like to thank the members of the technical team at Applied Energetics. Many members of the Tech Team contributed to this project–Eric and Kris built and worked on the laser, Iraj helped with the station setup, and I had many fruitful technical discussions about this project with them as well as my cube-mates Pedro, Brandin, and Kyle. I would like to extend thanks to Nate, who was an intern at the company during the summer of 2023; this guy was a huge part of many of the experiments that were required for this work. Also, I have to shout out Keeley for setting up many of the internal presentation days that kept me on track for the final stretch of this effort. Buddies, I like photonics a lot, but the hi-jinks and sillies of the day-to-day is really what kept me coming into the office and made this whole thing bearable. I owe you all many thanks on many levels, and this project never would have been completed without all of you.

I would like to thank the Dr. Gregory Quarles and the members of the administration at Applied Energetics. The administration showed no hesitation when they hired me on directly from an intern to a full time employee. Without the resources at AE, I would not have been able to prepare this report in the first place. I would like to extend special thanks to Dr. Alan Kost and Dr. Stephen McCahon. When I first showed up at Applied Optical Sciences, I was very green, to the point of not even knowing how a laser even worked in real life. These two men have been excellent mentors in my professional life and the path they led me down allowed me to grow from a complete novice into the person I am today. My gratitude for the investment these men made in me cannot be overstated and I only hope that I can one day be a mentor to others in the way that these two have been to me.

I would like to thank my family and friends. Graduate school has been a long six years, very tough at times. I had long phone calls with some of you. I drank (many) beers with some of you. I went on camping trips or trips out of the country with some of you. I played music with some of you. I spent holidays with some of you. You all had to hear about how I was 'almost done' with my degree for so many years. You all don't realize it, but you were all there for me at some point along in this journey. I am looking forward to spending more time with you all now that I am done with school.

Finally, I would like to extend special thanks my brother Alex, my mother Yolanda, and my father Charles. I was exposed to the many wonders of science

and mathematics from the time of my earliest memories. There was never anything I couldn't have if it was going to help me grow in my journey in my education. I remember my room was plastered with posters about the structure of the atom and the scientific method. I remember my mom would sit with my brother and I and we would recite the elements in the periodic table in order (until reaching chromium, which we thought was so funny that our laughter would often preclude us from continuing). I remember my dad would never let us miss one of the myriad extracurricular activities we were involved in growing up, no matter how much we complained. I remember my brother being there to suffer along with me and provide some comic relief whenever we were assigned (for reasons still unknown to me to this day) to do problems from some random algebra book or write a story that had a minimum page limit. This is it guys, it's all over, no more of this. You guys were here with me literally every step of the way, and I know it wasn't always easy to deal with me. I cannot thank you guys enough.

# Dedication

This work and all of the work that lead to it is dedicated to my parents Charles and Yolanda. I didn't understand how important school was until I was in the latter half of my twenties, and I am thankful that you two were there to shepherd and provide for me until I grew up. I love you guys.

# Contents

# Chapter 1

# Abstract

The use of laser direct-write methods in small-batch manufacturing has been going on for decades. One of the particularly useful applications of a direct-write method is for the fabrication of fiber Bragg gratings (FBGs). In this report, modeling and experimental results are presented for three fiber Bragg gratings that were fabricated in Newport F-SMF-28 fiber with the direct-write method. The model is based on coupled-mode theory assuming weakly guiding fibers. Details on qualitative investigations that drove the direct-write bench design and grating designs are discussed, as well as the methods by which the model and experimental results have been used to further improve the other. A discussion of the next steps of this investigation is featured at the end of the report.

The experiments described in this report were performed for the purpose of developing a lab tool that could be used to create fiber Bragg grating devices as internal research demands. In particular, there is an interest in the fabrication of FBGs for use in center wavelength selection for fiber master oscillator systems that are being built in-house.

# Chapter 2

# Introduction

The laser has proven to be an indispensable instrument in the world of manufacturing. Lasers have been used to perform a myriad of tasks in nearly every phase of general manufacturing processes: from processing raw bulk material, to evaluating the quality of a workpiece during or after production, to post-processing finished items. Lasers have inherent characteristics and large body of supporting tools in their periphery that make them particularly amenable for precision work: high power lasers with imaging systems allow for spot sizes below one micron and positioning stages with fidelity far below a micron are commonplace. The laser has also brought manufacturing to the laboratory–expensive industrial infrastructure is no longer required for small-batch fabrication benches, and many common research items can now be made in-house.

There are many manufacturing processes that are interesting in the laboratory setting, but among the most useful are direct-write processes, as they leverage the qualities that make lasers special–high spatial and temporal coherence–to a great degree, enabling the manufacture of passive devices relatively quickly to keep up with the rapid pace of requirement changes in research.

## 2.1 Direct-Write Methods

Direct-write methods use high peak power laser sources focused to small spots to make highly localized material modifications [1]. These modifications are typically characterized by a change in the refractive index of the exposed areas. The use of high power ultrashort pulses is what identifies direct-write methods among other laser manufacturing methods. This method is driven by nonlinear processes, and as such, it can be used to modify workpieces at subsurface levels, only limited by the working distance of the focusing system and the sensitivity of the substrate. This property is very useful for simplifying the manufacturing process of precise photonic devices; the need for complicated chemical etching or material deposition processes is completely circumvented in some cases. Instead, a substrate structure can be fabricated in bulk and modified later, which opens

the parameter space of devices that can be fabricated. Additionally, direct-write processes have the advantage of not requiring sensitized substrates; these methods can be applied even to inexpensive telecommunication fibers with a result that is of a fieldable quality. Devices that are produced in standard (not sensitized) substrates with the direct-write method do not suffer from the same erasure effects via heating that photonic devices produced with other methods (e.g. holographic methods) do; the written structures are more permanent.

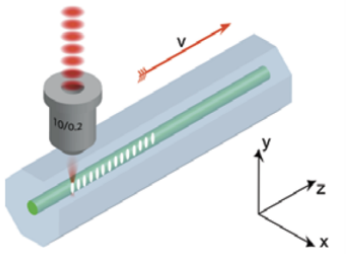


Figure 2.1: Diagram representation of a direct-write process taking place in an optical fiber, taken from Reference [2].

The intricacies of how ultrashort pulses modify substrates at the molecular level are difficult to fully encapsulate, as it seems there are many physical processes that take place when materials are irradiated with femtosecond pulses. There are publications that suggest that densification, strain, and changes in electronic structure play roles [1][3]. However, the effects are almost certainly attributable to multi-photon processes, either through field or avalanche ionization [4]. This allows lasers with lower photon energies (e.g. in the near-infrared) to be used as write sources; historically, ultraviolet sources were required to modify refractive index in photonic substrates. These sources are often very expensive and hard to get at high powers. Conversely, there is a large commercial base for ultrashort lasers around 800 nm (Ti:Sapphire) and 1030 nm (Ytterbium fiber or YAG) with turnkey operation. As an example, silica (the material that is the focus of this report) has a band gap energy of 8.9 eV [3], which corresponds to the energy of a single photon with a wavelength of 139 nm; however, an eight-photon process at 1030 nm also provides sufficient energy for an electron to cross the band gap, and it is through this (highly) nonlinear absorption that common material substrates are modified with near-infrared lasers.

For as complicated as the physical processes that underlie the direct-write method are, the practical implementation of the direct-write method is quite simple. The signal from a pulsed laser system is routed through an imaging (focusing) system to a workpiece that is placed on a fine linear and angular positioning stage setup. Coordination between the pulse signal timing and the positioning/speed of the positioning stages allows for the creation of write patterns that are useful for the fabrication of many different photonic devices. There are many options on the market for computer-controlled off-the-shelf positioning

stages with 10s of nanometer class precision. The space of realizable structures is only limited by the size of the focused laser spot and the positioning/speed fidelity of the stages being used.

The direct-write method can have extended fabrication times in certain configurations and sometimes suffers from shot-to-shot inconsistency for each of the writing laser pulses. Operating positioning stages at high speeds reduces their accuracy, so in addition to the limits on the linear speed of the workpiece translation apparatus per the device specifications, there are also more stringent practical limits on the speed at which a structure can be written that approximates its intended design characteristics. Care should be taken when specifying or designing a write laser to mitigate pulse energy fluctuations. While it is important to recognize these problems, the reader should note that they are reasonably easy to work around.

## 2.2 Description of Fiber Bragg Gratings

Fiber Bragg gratings (FBGs) are very common photonic devices that are deployed for a wide variety of applications across many fields–from their use in telecommunications in add-drop modules, to their use in sensor technologies for strain measurement (among other quantities), to their use in research for feedback elements in fiber lasers of all kinds. Fiber Bragg gratings enjoy the same benefits as other fiber devices; namely, they have a general insensitivity to alignment, they handle environmental perturbations rather well, and they deliver a higher beam quality compared to their free space counterparts. In addition, these devices are cheap to fabricate due in large part to the considerably-sized manufacturing base that exists for the production of optical fibers.

The most basic kind of fiber Bragg grating ideally features a sinusoidal index modulation function that is solely a function of the spatial argument corresponding to the axis of light travel in a waveguide structure, with planes perpendicular to the axis of light travel having a constant refractive index. These devices are characterized by a length $L$, a periodicity $\Lambda$, and an index modulation magnitude $\delta n$; these values are represented graphically in Figure 2.2. Many (but not all) of these basic devices act as 'mirrors' in optical fiber systems, and the grating periodicity, grating length, and the magnitude of the index modulation are the main factors that define the center wavelength and bandwidth of the reflection band.

A small step up in complexity allows for the creation of FBG devices that serve specific purposes. Chirped FBGs feature a grating period that changes with position along the direction of propagation, and these devices are used to stretch pulses in chirped-pulse amplification (CPA) architectures to enable fiber-monolithic high-energy laser builds. Phase-shifted FBGs feature a (mostly) constant grating period structure with discrete locations where there are periods with additional phase (achieved by modifying the length in a single period); these types of structures feature a narrowband transmission in the middle of the reflection band, which can be used for advanced filtering applications. Long-

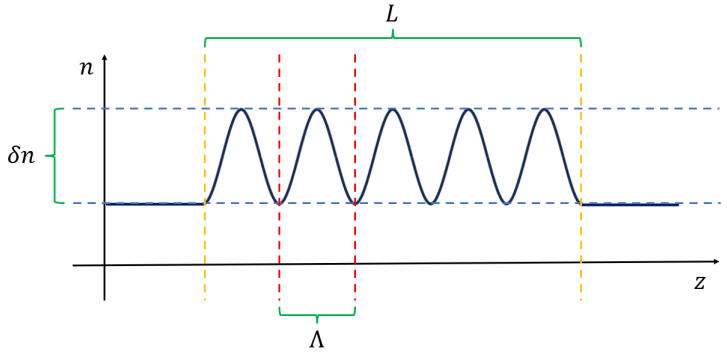


Figure 2.2: Diagram of a basic FBG index modulation function with variables labeled.

period FBGs can be used as filters as well; they are characterized by structures with periods in the neighborhood of 100 microns, and forward-couple light in the rejection band into the cladding, where it is coupled out of the system entirely. Tilted gratings serve a similar function; they feature tilted grating structures, and light in the rejection band is coupled directly out of the fiber.

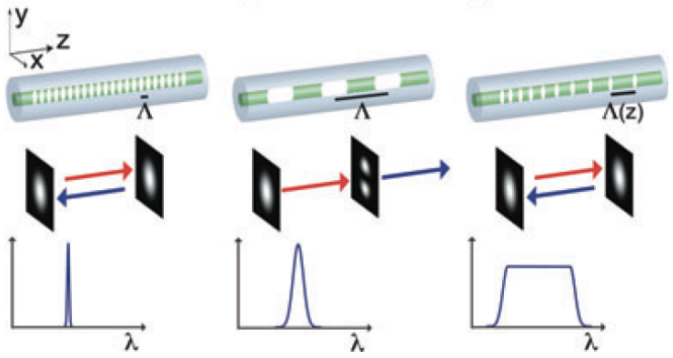


Figure 2.3: Examples of different FBG morphologies: a standard FBG (left), a long-period FBG (middle), and a chirped FBG (right), taken from Reference [2].

There has been a lot of work done to optimize the manufacture of FBGs. Much of this work has been fruitful, and these devices enjoy the luxury of having robust and reasonable production methods at any scale–from the manufacture of thousands of them in quick succession in large industrial setups to single units used for one-off laboratory experiments. A practical and useful application of the direct-write method in a laboratory setting is for the creation of fiber Bragg grating devices on demand. These devices are simple in concept and the

substrate materials are cheap; single-mode telecommunication fiber has a price in the neighborhood of a dollar per meter at the time of the writing of this report. The manufacture of these devices in house is more than just a parlor trick, as these devices can command high prices with long lead times if the required FBG has properties that deviate from commonly requested configurations (e.g. seldom used wavelengths, specialty fibers, etc.). A well-behaved direct-write setup can produce a wide variety of fiber gratings useful for many applications at times on the order of a day and at a fraction of the price demanded by a company issuing a custom quote.

## 2.3 Report Summary

The impetus for the effort described in this report was to create a laboratory laser direct-write bench setup for the production of fiber Bragg grating devices that could be used to set the wavelength of master oscillator systems that are built in-house.

The first subject of this report is the theory of fiber Bragg gratings. The first section of this document will be a brief overview of optical fibers, as the qualities they exhibit are critical to the operation of FBG devices. The topic of the second section is the mathematical analysis of FBGs; a short word will be made on the breadth of analysis techniques available to the interested party, but an emphasis will be placed on coupled-mode theory. This information is intended to be concise: emphasis will be presented with a focus on results as opposed to full derivations; references will be provided that do present the full derivations for the presented results.

The third section will present the fabrication results of three separate FBG devices, going into detail with regards to the method of fabrication and presenting a comparison of the output of the modeling effort and the test data. Additionally, details on the bench setup, the methods of model calibration, and some of the qualitative behavior exhibited in the experiment will be discussed.

# Chapter 3

# Signals in Optical Fibers

Before talking specifically about FBGs, it is necessary to discuss some of the properties signals in optical fibers, in both a physical and mathematical sense.

## 3.1 Structure of Optical Fibers

Optical fibers come in many different shapes and sizes, but the most common fibers (telecommunication fibers, fibers for common-wavelength fiber lasers) feature a cylindrical glass core with a constant refractive index (denoted by $n_{co}$) surrounded by a cylindrical glass cladding with a slightly lower refractive index (denoted by $n_{cl}$).

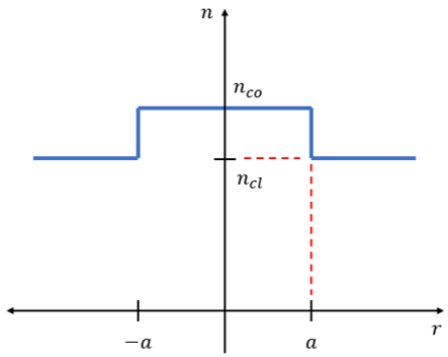


Figure 3.1: Diagram of the index profile of a single-mode fiber.

From a practical standpoint, the waveguiding behavior of optical fibers can be understood from a ray treatment of light with total internal reflection in the core structure; in this way, it is intuitive as to why the core must have a higher index than the cladding for the fiber to guide light. Further mathematical analysis must be used to understand the behavior from a wave optics

perspective.

In an ideal fiber, these two cylinders are perfectly concentric, and the radius of the cladding is typically much greater than the radius of the core. Proper sizing of the cladding region allows for limited influence of the cladding structure on the modes propagating in the core. These glass cylindrical structures are surrounded by a polymer layer (also cylindrical and ideally concentric with the other two cylindrical structures) that is used to provide additional mechanical rigidity and durability. The polymer jacket is a structure with a lower refractive index than the cladding that attenuates signals propagating in the cladding. Certain fibers feature a polymer that allow for the cladding to guide as well, but these types of fibers are not discussed in this document.

Most standard optical fibers are made of silicon dioxide (also known as 'fused silica' or just 'silica'); nearly all telecommunication fibers are of this type. Silica is used chiefly because is in inexpensive, it has good mechanical properties, it does not react with common chemical compounds in the environment, and it is transparent in the near-infrared spectral region. The excellence of silica as an optical material caused many laser systems and their supporting technologies to be developed specifically to accommodate the transmission characteristics of silica. Modern manufacturing technology has allowed for the production of silica fibers that have very low attenuation around 1550 nm, as low as 0.2 dB/km [5]. To increase the refractive index in the core, the silica host is doped with a small percentage of germanium dioxide in the manufacturing process, which has a higher bulk refractive index than silica. Other materials are used in the manufacture of optical fibers for handling different spectral regions; for instance, silica is not appropriate for signals in the mid-infrared region, as it is too absorptive. The key in finding the right fiber for the application is often just about the transparency of the fiber material at the signal wavelength in question.

A basic property of a fiber worth mentioning is called numerical aperture (NA). It is defined as the following:

$$NA = \sqrt{n_{co}^2 - n_{cl}^2} \tag{3.1}$$

The numerical aperture of a fiber is analogous to the numerical aperture of an optical system, but the two values are not the same. They both refer to the ability of an the fiber or system to accept incoming light. However, the numerical aperture of an optical system refers to an entire bundle of rays that the system will accept, whereas for a single-mode fiber, the numerical aperture describes the one "ray" that will be accepted by the system. For full power coupling into the fiber, the incoming beam must exactly be characterized as having the divergence angle corresponding to the fiber numerical aperture or there will be loss. Multimode fibers have similar behavior; they have a set of multiple discrete "rays" that will couple into the fiber.

## 3.2 The Wave Equation

Like all other electromagnetic phenomena, the understanding of how signals propagating in optical fibers behave starts with Maxwell's Equations. They are discussed briefly in this section, as any report in the periphery of optical physics is incomplete without them.

Maxwell's Equations for a medium that is non-magnetic and without source charges or currents (as is the case for effectively all optical fibers) are stated as follows [6]:

$$\nabla \cdot \mathbf{D} = 0 \tag{3.2}$$

$$\nabla \cdot \mathbf{B} = 0 \tag{3.3}$$

$$\nabla \times \mathbf{E} = -\frac{\partial \mathbf{B}}{\partial t} \tag{3.4}$$

$$\nabla \times \mathbf{H} = \frac{\partial \mathbf{D}}{\partial t} \tag{3.5}$$

With the following definitions of the variables:

- $\mathbf{E}$ is the electric field vector
- $\mathbf{H}$ is the magnetic field vector
- $\mathbf{D}$ is the electric displacement flux vector
- $\mathbf{B}$ is the magnetic displacement flux vector

In the statements above, variables in **bold** are representative of vector quantities, and this convention will be used throughout the rest of this document.

Additionally, there are relationships between some of the variables in the equations, called the constitutive equations. If we add the constraint that the system must be operating in a linear regime (meaning that the field amplitude is small such that the onset of nonlinear behavior is negligible) to the set of assumptions made about the system, we can state the constitutive equations as such:

$$\mathbf{D} = \epsilon_0 \mathbf{E} + \mathbf{P} = \epsilon_0 \epsilon_r \mathbf{E} \tag{3.6}$$

$$\mathbf{B} = \mu_0 \mathbf{H} \tag{3.7}$$

where:

- $\mathbf{P}$ is the material polarization
- $\epsilon_0$ is the vacuum permittivity
- $\epsilon_r$ is the relativity permittivity of the material
- $\mu_0$ is the vacuum permeability

From Maxwell's Equations, a Wave Equation can be derived and subsequently solved that sets conditions for a class of physically-realizable fields (harmonic-wave solutions) must meet.

$$\nabla^2\mathbf{E} - \frac{n^2}{c_0^2}\frac{\partial^2\mathbf{E}}{\partial t^2} = -\nabla(\mathbf{E}\cdot\nabla \ln n^2) \tag{3.8}$$

Note that $n = \sqrt{\epsilon_r}$ and $c_0 = \frac{1}{\sqrt{\epsilon_0\mu_0}}$.

Equation 3.8 is a vector equation [7]. The term on the right-hand side of this equation arises because the permittivity of the systems being examined in this document (optical fibers) have spatial dependence on the transverse coordinates. This form will not be examined in this report; it is stated just for completeness.

At this point in the analysis, the modal field profiles of a fiber are derived by assuming that there is a discrete spatial wavenumber (represented in this document and most of the literature as $\beta$) associated with a field's propagation through a waveguide along the direction of propagation. Mathematically, this amounts to assuming solutions of the form [8]:

$$\mathbf{E}(r,\phi,z,t) = (\mathbf{E}_t(r,\phi) + E_z(r,\phi)\hat{\mathbf{z}})\exp\left[i(\omega t - \beta z)\right] \tag{3.9}$$

where:

- $\omega$ is the temporal angular frequency of the mode being expressed
- $\beta$ is the spatial wavenumber of the mode being expressed
- $\mathbf{E}_t(r,\phi)$ is the transverse mode field profile
- $E_z(r,\phi)$ is the longitudinal mode field profile (note that this function is scalar)

Note also that $r = \sqrt{x^2+y^2}$ is the radial coordinate and $\phi = \arctan(y/x)$ is the azimuthal coordinate; the above equations are stated in cylindrical coordinates to accommodate the geometry of optical fibers.

Due to the linear nature of Maxwell's Equations, each of the signal's spectral elements can be examined individually, and their contributions can be summed up to model the total behavior of the system. Note that this is only true when the devices are not being analyzed using very high signal powers, which would require analysis of nonlinear behavior. This would in general mean that there is coupling between different spectral components.

To solve for the modal fields, the Wave Equation (Equation 3.8) must be solved subject to the boundary conditions for Maxwell's Equations at a cylindrical surface; these conditions are as follows [6]:

- The tangential components of the electric ($\mathbf{E}$) and magnetic ($\mathbf{H}$) fields must be continuous at the boundary
- The perpendicular components of the electric displacement ($\mathbf{D}$) and magnetic displacement ($\mathbf{B}$) fields must be continuous at the boundary

Solving the Wave Equation with cylindrical boundary conditions characteristic of optical fibers gives the modal fields.

## 3.3 A Useful Parameterization of Fiber Characteristics

Before continuing, it is useful to introduce the concept of normalized fiber parameters–the bV-parameters [8]. Like most normalization schemes, it is useful to define these parameters because they allow for very general statements about system characteristics they represent, and they can alleviate some of the problems that arise when working with large numbers in numerical calculation processes.

The parameters are defined as follows:

$$b = \frac{N_{eff}^2 - n_{cl}^2}{n_{co}^2 - n_{cl}^2} \tag{3.10}$$

$$V = ka\sqrt{n_{co}^2 - n_{cl}^2} \tag{3.11}$$

where:

- $N_{eff}$ is the effective index for the signal frequency under examination
- $k$ is the vacuum wavenumber of the signal frequency under examination
- $a$ is the radius of the fiber core

The parameter $b$ is called the normalized index and the parameter $V$ is called the normalized frequency. The effective index can be thought of as defining the modal velocity (analogous to what would be the 'phase velocity') of the mode being examined; it has the following relationship to the spatial wavenumber $\beta$:

$$\beta = kN_{eff} \tag{3.12}$$

The value of $b$ is always between zero and one. Knowledge of this characteristic and the mathematical definition of $b$ implies a physical truth: the effective index will always be between the value of the core index and the cladding index. Modes that correspond to higher $b$ values have fields that are more well-confined in the fiber core and have modal velocities that approach the bulk phase velocity in the core (defined by $n_{co}$); modes that are weakly-confined have lower $b$ values and have modal velocities that approach the bulk phase velocity in the cladding (defined by $n_{cl}$).

The $V$ value can be used to determine the modal volume of the fiber in question at the (temporal) signal frequency being examined. As the value of $V$ increases, the number of modes corresponding to that value of $V$ that are guided by the fiber also increases. In particular, a fiber is single-mode (i.e. it only guides the fundamental mode) if $V < 2.405$ (approximately).

## 3.4 Analytical Forms of Modal Fields

The analytical forms of the fiber modal fields will be stated in terms of the bV-parameters described in the previous section.

For the interested party, the vector modal fields of a dielectric cylindrical geometry were solved for by Snitzer [9] many decades ago. The mathematical procedure is at times very arduous, but the results are exact. However, for the analysis performed in this document, the use of the vector modal fields is unnecessary. The modal behavior of optical fibers can be simplified (while still maintaining a high degree of accuracy with respect to actual fiber modal behavior) is by use of the weakly-guiding approximation [10], which is valid under the following condition:

$$\Delta = \frac{n_{co} - n_{cl}}{n_{co}} \ll 1 \tag{3.13}$$

The above expression implies that the index contrast between the core and the cladding must be small for the weakly-guiding approximation to be employed. Fortunately, this is generally the case for common optical fibers. Fibers that meet the criteria in Equation 3.13 also exhibit approximately linearly-polarized behavior for individual modes guided by the fiber–the full set of these modes make up what are called the linearly polarized (LP) modes. In reality, these modes are sums of the vector modes that happen to approach linearly-polarized behavior as certain sets of the vector modes approach the same modal velocities. This occurs as the index contrast between the core and cladding of a fiber decreases. In this regime, the magnitude of the longitudinal field is much smaller than the magnitude of the transverse field. Chapter 9 of Reference [8] features an excellent discussion of this behavior.

In literature, the linearly polarized modes are designated with the convention $LP_{lm}$. The subscript $l$ is used to denote the azimuthal order of the mode; the value of $l$ must be an integer value greater than or equal to zero. The subscript $m$ is used to denote the radial order of the mode; the value of $m$ must be an integer value greater than or equal to one. The $LP_{lm}$ mode has $2l$ azimuthal field zeros and $m-1$ radial field zeros.

The modal fields for a fiber under the weakly-guiding approximation are expressed as follows [8]; first, for the field in the core ($r \leq a$):

$$\mathbf{E}_t(r,\phi) = e_{co}(r)\cos(l\phi)\hat{\mathbf{x}} \tag{3.14}$$

$$e_{co}(r) = C_l^{co}\frac{J_l\left(V\sqrt{1-b}(\frac{r}{a})\right)}{J_l\left(V\sqrt{1-b}\right)} \tag{3.15}$$

then, for the field in the cladding ($r > a$):

$$\mathbf{E}_t(r,\phi) = e_{cl}(r)\cos(l\phi)\hat{\mathbf{x}} \tag{3.16}$$

$$e_{cl}(r) = C_l^{cl}\frac{K_l\left(V\sqrt{b}(\frac{r}{a})\right)}{K_l\left(V\sqrt{b}\right)} \tag{3.17}$$

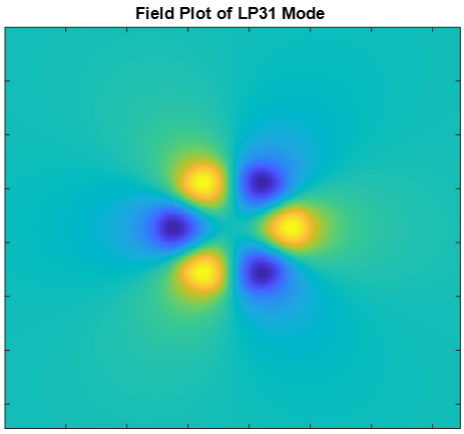


Figure 3.2: Field plot of the $LP_{31}$ mode; the yellow areas represent field values in the positive x-direction and the blue areas represent field values in the negative x-direction.

where:

- $C_l^{co}$ and $C_l^{cl}$ are values dependent on mode field strength
- $J_l$ is the Bessel function of the first kind of order $l$
- $K_l$ is the modified Bessel function of the second kind of order $l$

In his paper [10], Gloge assumes the forms of the modal field defined in Equations 3.14 and 3.15 and describes a process by which it can be shown that the weakly-guided transverse fields are recoverable under the application of Maxwell's curl equations [11] to a degree of accuracy of order $\Delta$ defined in Equation 3.13.

The value of $C_l^{co}$ and $C_l^{cl}$ only depends on the value of mode field strength as it is stated in Equations 3.15 and 3.17; there is a normalization process that generalizes these values that will be discussed in the next section.

For completeness, the form of the longitudinal field (along the direction of propagation) will be stated [8], as it is important for some modeling applications regarding LP modes. However, the reader should note that these equations will not be used for the remainder of the analysis in this document. The longitudinal field in the core ($r \leq a$) is:

$$E_z(r,\phi) = -\frac{i}{\beta}\left[\frac{de_{co}(r)}{dr}\cos(l\phi)\cos(\phi) + \frac{l}{r}e_{co}(r)\sin(l\phi)\sin(\phi)\right] \tag{3.18}$$

analogously, the longitudinal field in the cladding ($r > a$) is:

$$E_z(r,\phi) = -\frac{i}{\beta}\left[\frac{de_{cl}(r)}{dr}\cos(l\phi)\cos(\phi) + \frac{l}{r}e_{cl}(r)\sin(l\phi)\sin(\phi)\right] \tag{3.19}$$

At this point, the only thing that remains to be done to calculate the fiber modal fields is to calculate $b$ for each value of $V$; thus, the relationship between these values must be defined. This is done by applying the boundary conditions for Maxwell's Equations (specifically, functional continuity of the tangential component of the **E** field at the boundary) to Equations 3.14 and 3.16. The boundary conditions give rise to what is called the eigenvalue equation for weakly-guiding fibers [8]. The equation is stated below:

$$V\sqrt{1-b}\frac{J_{l+1}(V\sqrt{1-b})}{J_l(V\sqrt{1-b})} = V\sqrt{b}\frac{K_{l+1}(V\sqrt{b})}{K_l(V\sqrt{b})} \tag{3.20}$$

Another result of the application of the boundary conditions is that the weighting terms in the expressions of the fields (Equations 3.14 and 3.16) must be equal; that is, $C_l^{co} = C_l^{cl}$. Chapter 9 of Reference [8] provides a description of the mathematical process required to arrive at these results.

The dispersion curve for a fiber can be calculated by first solving the eigenvalue equation (Equation 3.20) for $b$ at all values of $V$ that the signal temporal frequency domain (analogous to wavelength domain) requires. Once the user has the equation solved in terms of the bV-parameters, they only have to specify the core refractive index, the cladding refractive index, and the fiber core radius to state the dispersion relation in the form $\beta(k)$, which is the generally accepted definition of the dispersion relation used to define other parameters that are commonly used in physics or engineering discussions in the periphery of optical fibers.

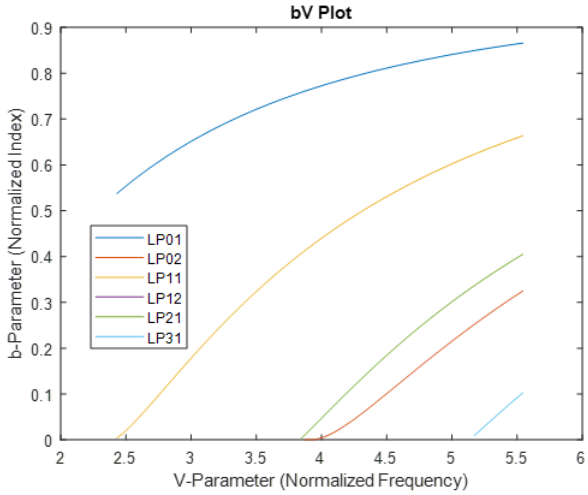


Figure 3.3: The bV plot for values of V between 2.4 and 5.6 for the six lowest-order LP modes.

Equation 3.20 is not analytically solvable and thus the value must be derived numerically. For multimode fibers, the reader should note that Equation

3.20 permits multiple solutions at some of the wavelengths in the spectral domain being analyzed. Care should be taken when using pre-packaged numerical software to not neglect these solutions, as they form the dispersion curve for higher-order modes.

Once the eigenvalue for the mode in question is calculated, the modal profile can be expressed by substituting the eigenvalue into parameter $\beta$ in Equations 3.14 and 3.16.

## 3.5 Full Expression of Fiber Fields

Under the weakly-guiding approximation, the discrete (guided) modal fields form an orthogonal basis [12]. For the expression of arbitrary transverse field profiles, the radiation modes must also be included, which are a continuum of fields that are not guided by the fiber [13]. An example of such a field is one that would enter the fiber at an angle, refract in the core structure, and immediately couple out. However, for well-guided signals in weakly-guiding fibers of constant diameter, the radiation modes can be ignored, as they represent a very small part of the fields in these fibers (likely arising because of small manufacturing imperfections). Thus, arbitrary fields in the fibers can be (approximately) expressed with the following equation [12]:

$$\mathbf{E}_t = \frac{1}{2}\sum_{\mu=1}^{q}\{A_\mu(z)\xi_{\mu t}\exp\left[i(\omega t - \beta_\mu z)\right] + c.c.\}\hat{\mathbf{x}} \tag{3.21}$$

where:

- $q$ is the total number of LP modes guided by the fiber
- $A_\mu$ is the functional weight of the $\mu$-th mode
- $\xi_{\mu t}$ is the normalized modal field of the $\mu$-th mode (the $t$ subscript denotes that the field is transverse)
- $\beta_\mu$ is the spatial wavenumber associated with $\mu$-th mode
- *c.c.* is the complex conjugate

The expressions of the modal fields that are normalized according to the following relationship:

$$\frac{1}{2}\left(\frac{\beta_\mu}{\omega\mu_0}\right)\iint \xi_{\mu t}\cdot\xi^*_{\nu t}dxdy = \delta_{\mu\nu} \tag{3.22}$$

Where $\delta_{\mu\nu}$ is Kronecker delta. The condition described in Equation 3.22 allows for the power in the $\mu$-th mode to be calculated with $|A_\mu|^2$. These normalized fields will be used later in the section where the coupled-mode equations are discussed.

# Chapter 4

# Mathematical Analysis of Fiber Bragg Gratings

There are many methods of analyzing the behavior of FBGs, but for the purpose of this document, attention will be given specifically to the coupled-mode treatment. The reader will see that this method is compact and intuitive, and there is a large body of data that suggests that this level of analysis is sufficient for a meaningful prediction of the behavior of an FBG.

## 4.1 Phase Matching

The basic mathematical concept that describes the first-order behavior of FBGs is what is known as phase matching. This statement is ultimately derived from the grating equation [14], but will be stated below without derivation for brevity:

$$\beta_\mu = \frac{2\pi N}{\Lambda} \pm \beta_\nu \tag{4.1}$$

where the variables are defined as follows:

- $\beta_\mu$ is the spatial wavenumber of the $\mu$-th mode of the system
- $N$ is the order number of the grating, which must be an integer
- $\Lambda$ is the length of one period of the grating

For basic grating design, the wavenumbers (which are defined as they were in the previous section) of two signal modes that are to be coupled can be calculated, the order of the grating can be assumed, and the periodicity of the grating can be specified. Use of the 'plus' in Equation 4.1 corresponds to phase matching of counter-propagating modes (the case of a reflective grating), where use of the 'minus' in the equation corresponds to phase matching of co-propagating modes (in the case of a forward-coupling grating). For the greatest transfer of

energy between two modes being analyzed, the phase matching condition must be met.

The phase mismatch ($\Delta\beta$) of two signal modes for a given grating order and periodicity is defined with the following equation:

$$\Delta\beta = \beta_\nu \pm \beta_\mu - \frac{2\pi N}{\Lambda} \tag{4.2}$$

This value is an analog to detuning behavior and degrades the efficiency of coupling as it increases. The use of 'plus' or 'minus' in Equation 4.2 follows the same convention as the one used in Equation 4.1. This definition will be used in the discussion of the coupled-mode equations.

## 4.2 Coupled-Mode Analysis

The purpose of this section is to give the reader a sufficient amount of information so they have all the tools necessary to understand the basic components of a grating model and begin a model of their own. A full step-by-step derivation of the coupled-mode equations from the wave equation is quite involved and beyond the scope of this document. The reader is encouraged to look at Chapter 4 of Reference [12] where the derivation is presented in a complete and logical way. The convention used for this section of the document is very similar to the convention used by R. Kashyap. It should be noted that this reference guided much of the work done for this entire endeavor; it is an excellent piece of literature.

The coupled-wave equations for a forward and backward propagating wave are stated as follows [12]:

$$\frac{dR}{dz} + i\left[\kappa_{dc} + \frac{1}{2}\left(\Delta\beta - \frac{d\phi(z)}{dz}\right)\right]R = -i\kappa_{ac}^{*}S \tag{4.3}$$

$$\frac{dS}{dz} - i\left[\kappa_{dc} + \frac{1}{2}\left(\Delta\beta - \frac{d\phi(z)}{dz}\right)\right]S = i\kappa_{ac}R \tag{4.4}$$

where

$$R = A_\nu \exp\left[-\frac{i}{2}(\Delta\beta z - \phi(z))\right] \tag{4.5}$$

$$S = B_\mu \exp\left[\frac{i}{2}(\Delta\beta z - \phi(z))\right] \tag{4.6}$$

In the equations above, the variables $R$ and $S$ are representative of the forward and backward propagating modes, respectively. This follows convention, where the forward propagating wave is referred to as the "reference" and the backward propagating wave is referred to as the "signal" (this convention is specifically used for reflective gratings). The $\nu$ and $\mu$ subscripts denote the modal index; the different variables are used to emphasize that the two modal

fields do not necessarily have to correspond to the same mode. The other variables are defined as follows:

- $\Delta\beta$ is the phase mismatch
- $\phi(z)$ is the position dependent local phase of the index modulation function
- $\kappa_{dc}$ is the system dc coupling coefficient
- $\kappa_{ac}$ is the system ac coupling coefficient

The definition of the dc and ac coupling coefficients are as follows:

$$\kappa_{dc} = n\omega\epsilon_0 \int \overline{\Delta n} \xi_{\mu t} \xi^*_{\mu t} dxdy \tag{4.7}$$

$$\kappa_{ac} = n\omega\epsilon_0 \int \frac{\Delta n}{2} \xi_{\nu t} \xi^*_{\mu t} dxdy \tag{4.8}$$

where the variables are defined as follows:

- $\omega$ is the angular frequency of the signal under inspection
- $n$ is the refractive index of the unperturbed grating medium at frequency $\omega$
- $\overline{\Delta n}$ is the average value of the refractive index modification function in a single grating period (the DC index change)
- $\Delta n$ is the value of the amplitude of the index modification function around the average value (the AC index change)
- $\xi_{\mu t}$ is the normalized modal field of the $\mu$-th mode (the $t$ subscript denotes that the field is transverse)

In the equations above, the integral extends over all transverse (orthogonal to the direction of propagation) space. Recognizing that the $\mu$ subscript corresponds to the backward-propagating (reflected) signal and the $\nu$ subscript corresponds to the forward-propagating signal, it is apparent that the magnitude of the dc coupling coefficient is based only on the mode-field profile of the reflected signal. In contrast, the magnitude of the ac coupling coefficient is dependent on both the forward- and backward-propagating fields.

A useful relationship between $\Delta n$ and $\overline{\Delta n}$ is the following:

$$\Delta n = v\overline{\Delta n} \tag{4.9}$$

where $v$ is the visibility for the modifications. Visibility is defined as:

$$v = \frac{n^{mod}_{max} - n^{mod}_{min}}{n^{mod}_{max} + n^{mod}_{min}} \tag{4.10}$$

In Equation 4.10, $n^{mod}_{max}$ and $n^{mod}_{min}$ are the maximum and minimum values of the index modification function in the grating, respectively. This equation

implies that the minimum value of the index in the grating structure is not necessarily the index value of the unmodified substrate; this is a scenario that arises when the modifications are not spaced appropriately and thus have some degree overlap.

For reference, Figure 4.1 shows the graphical representation of some of the variables discussed in this section.

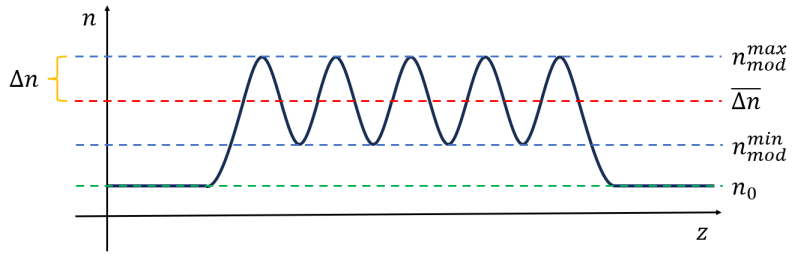


Figure 4.1: Graphical representation of some of the relevant variables for coupled-mode analysis. Note here that $n_0$ represents the unmodified value of the refractive index.

Finally, the coupled-mode equations as stated in this section permit an analytical solution for the reflection coefficient $\rho$ as follows:

$$\rho = \frac{-\kappa_{ac}\sinh(\alpha L)}{\delta\sinh(\alpha L) - i\alpha\cosh(\alpha L)} \tag{4.11}$$

where the variables $\delta$ and $\alpha$ are defined with the following expressions:

$$\delta = \kappa_{dc} + \frac{1}{2}\left(\Delta\beta - \frac{d\phi(z)}{dz}\right) \tag{4.12}$$

$$\alpha = \sqrt{|\kappa_{ac}|^2 - \delta^2} \tag{4.13}$$

This result is returned when the value of the derived signal function at the beginning of the grating domain is divided by the value of the derived reference function at the beginning of the grating domain; that is, $\rho = \frac{S(0)}{R(0)}$. The initial conditions used to arrive at this result are as follows: the forward-propagating wave is assumed to have a normalized field value of one at the beginning of the grating structure (stated mathematically, $R(0) = 1$) and the backward-propagating wave is assumed to have a normalized field value of zero at the end of the grating structure (stated mathematically, $S(L) = 0$ for a grating of length $L$). This makes logical sense, as the incoming field is full strength at the beginning of the grating and the reflected field does not exist at the end of the grating.

Equation 4.11 is the most important result for this section, and can accommodate most basic fiber Bragg grating geometries. It can be squared to return the power reflectivity value.

A notable special case of this equation is for when $\delta$ approaches zero, a condition that arises when $\kappa_{dc}$ and $\Delta\beta$ both approach zero in an unchirped ($\phi(z)$ is constant) grating. For gratings that exhibit these qualities, the reflection behavior is expressed with Equation 4.14.

$$|\rho|^2 = \tanh^2(\kappa_{ac}L) \tag{4.14}$$

If not already recognized, the reader should note that the coupled-mode equations (Equations 4.3 and 4.4) are stated for a single optical frequency for a single index modulation frequency. For the behavior of a system composed of index perturbations expressible with multiple spatial frequencies (for example, when using Fourier Series decomposition to analyze more complex structures), the coupled-mode equations have to be solved for each spatial frequency component at each optical frequency component. The resulting calculated reflection coefficients can be summed to determine the aggregate system behavior; this is again a consequence of the system being linear.

## 4.3 Analysis of Parameter Variations

There are a number of variables that can be altered during grating fabrication to give rise to different grating behavior. The discussion in this section of the report will focus on three: the grating periodicity, the grating region length, and the magnitude of $\Delta n$.

The modification of grating periodicity changes the phase-matching behavior of the system, and consequently, the center wavelength of the reflection band. General changes in band center behavior are described with the phase mismatch equation (Equation 4.2). In reality, the calculation of the full reflectivity function is still necessary to determine the full effect of periodicity change on the system, as there are subtle changes that arise in the behavior for each of the system spectral components.

The modification of the grating length has a less obvious effect on the system: it is related to both the magnitude of the reflection coefficient and the width of the reflection band. As it is a single parameter that affects both values, it alone cannot be changed to produce arbitrary values of both reflection amplitude and bandwidth. Typically, gratings that have shorter spatial extent have lower reflection magnitudes with larger bandwidths; longer gratings have higher reflection magnitudes with a narrower bandwidth.

Eventually this general relationship breaks down as the length of the device gets longer; the reflection function approaches top-hat behavior with the magnitude approaching unity and the bandwidth approaches a terminal value.

A change in the value of $\Delta n$ also has an effect on the amplitude of the reflection coefficient; higher values of $\Delta n$ are correlated with higher reflection values. However, the bandwidth also increases with an increase in this value; in this way, it acts differently than an increase in length.

There is also a shift in the center wavelength of the device with an change in $\Delta n$. This shift can be significant with even small changes, so the effect cannot

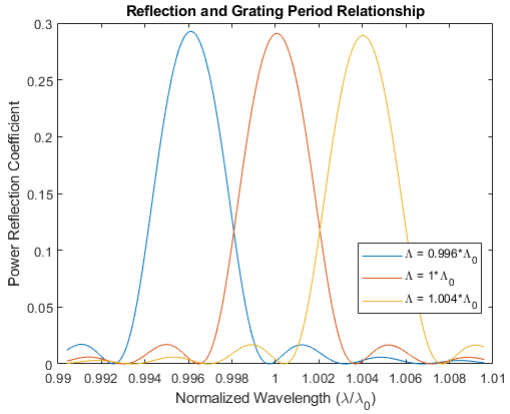


Figure 4.2: Plot showing effect of changing normalized grating period on reflection band behavior.

be ignored.

As the value of $\Delta n$ increases, the maximum reflectivity tends towards a value of unity like an increase in length, and the reflectance function similarly begins to exhibit top-hat like behavior. However, the bandwidth can continue to grow with an increase in $\Delta n$.

Alterations to the three values discussed in this section allow for a degree of design tunability with regards to center wavelength, bandwidth, and maximum reflection value. Combinations of changes to these parameters allow for mitigation of behaviors such as the decrease in reflection amplitude when attempting to increase the bandwidth by shortening the grating. To a certain degree, the decrease in the reflection function amplitude can be remedied by increasing the value of $\Delta n$, through inducing a higher value index modification or increasing the visibility of the grating structure. The interested party just has to ensure that the design they have arrived at is physically realizable.

On a final note, in addition to altering the reflection amplitude characteristics, the change of any of these parameters also has an effect on the phase characteristics of the reflection. If the signals that are being analyzed are pulsed, these changes will have effects on the temporal character of the pulse. These effects may or may not be significant for the application at hand but do need to be considered in device analysis.

## 4.4 A Brief Word on Other Modeling Methods

If there is a local periodicity to the FBG under study, the transfer matrix method is an appropriate method of breaking down the behavior of the structure as a whole. The analytical solution of the coupled-mode equations can be solved for each section of the device with constant period and represented as matrix

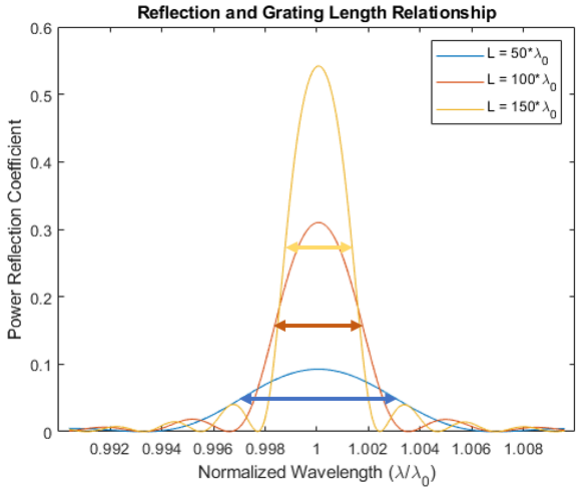


Figure 4.3: Plot showing effect of changing normalized grating length on reflection band behavior. Arrows are visual representations of the FWHM and are color coded to their respective length functions.

operators that encode the reflection magnitude and phase behavior of each spectral component. The product of the operators of each structure describes the behavior of the whole system. There are mathematical considerations to be made when sectioning the structure into smaller periods; the sections cannot be arbitrarily small (i.e. one grating period long) and still return a result that approximates reality. The mathematical limits of this method still permit its use for a large set of problems of interest, and if they are adhered to, meaningful results can be obtained.

A variation of Rouard's method [15], which was originally developed for analysis of microwave devices, can be used to model fiber Bragg gratings. This method involves 'slicing' the FBG under investigation in the spatial domain along the direction of propagation and calculating the reflectivity and transmission of each of these slices. The characteristics of each of the slices are represented as matrix operations in a similar way to the transfer matrix method described above, and analogously the product of these operators describes system-level behavior. This method can be applied at the grating period level and can also handle the full three-dimensional expression of index profiles. Results give an accurate description of complex grating structure behavior, but there is potentially a substantial increase in requisite computing power to be able to use this method.

If all else fails, the coupled-mode equations can be numerically integrated for arbitrary waveguide shapes, grating phase profiles, and modulation depth spatial profiles. This would require the use of numerical mode solvers (for arbitrary transverse field profiles), boundary-value problem solvers (e.g. use

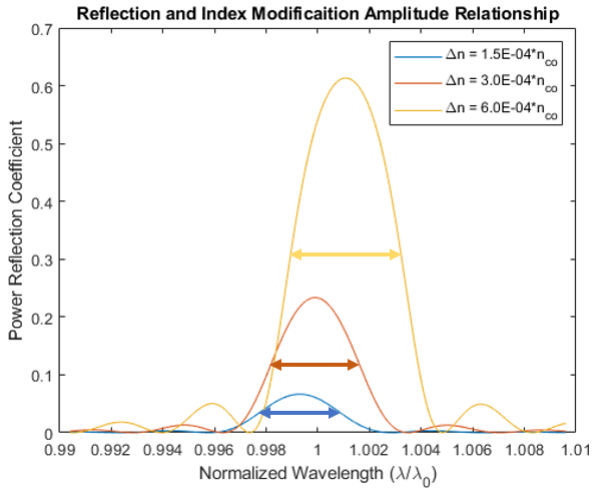


Figure 4.4: Plot showing effect of changing normalized magnitude of the index modification on reflection band behavior. Arrows are visual representations of the FWHM and are color coded to their respective length functions.

of a shooting method, a relaxation method, etc.), and a computer that has the appropriate power. The user only has to consider the cost-benefit analysis of the time they would like to wait and the required precision of the answer they seek.

# Chapter 5

# Analysis and Characterization of Real FBG Devices

This section details the process by which three specific fiber Bragg gratings (very important milestones for this effort) were fabricated and characterized. The process featured a back-and-forth relationship between the modeling and experimental steps. First, the fabrication and testing equipment had to be configured such that experimental writes were consistently yielding results that were behaving; this required an exploration where many basic experiments were performed to determine practical limits on the system performance. Once these limits were found, writes were performed until a pair of devices (SCRIBE055 and SCRIBE056) were demonstrated that had characteristics that approximated those of some of the designs that were examined in the initial exploration of the parameter space. This data was used to calibrate the model, and the model was used (with some assumptions about the index modification process) to design a third grating (SCRIBE057) with different characteristics than the first two. This device was fabricated and served as another calibration point for the model.

## 5.1 Fabrication and Testing Equipment Features

The write source used in the fabrication process featured a fiber master oscillator-power amplifier architecture (fully polarization-maintaining) with a free-space grating compressor at the output. The master oscillator (MO) output was pulsed at a 50 MHz repetition rate, had an average power output of 450 mW, was centered spectrally at approximately 1032 nm, and had a bandwidth of about 14 nm. The signal was reported on the datasheet to be verifiably compressible to under 200 fs, but the output was chirped to about 25 ps so that it could be amplified directly without any additional stretching. The MO output

was pulse-picked down to a repetition rate of about 1 MHz, and this signal was amplified in a two-stage Yb-doped fiber amplifier chain featuring a smaller double-clad 10/125 fiber pre-amplifier and a larger 25/250 double-clad fiber power amplifier. The output of the power amplifier was collimated and traveled through a double-pass grating compressor that included a pair of 1200 lp/mm dielectric transmission gratings and a roof prism. The output signal pulse duration was minimized experimentally using a thin second-harmonic generation crystal; the exact duration was not measured but was estimated to be below a picosecond based on the bandwidth and compression technique used. The output was usable between about 100 mW and 1 W average power (100 nJ and 1 uJ pulse energy, measured at the output of the compressor) before the write signal began to suffer from incompressibility, likely due to the onset of nonlinearities in the fiber amplifiers.

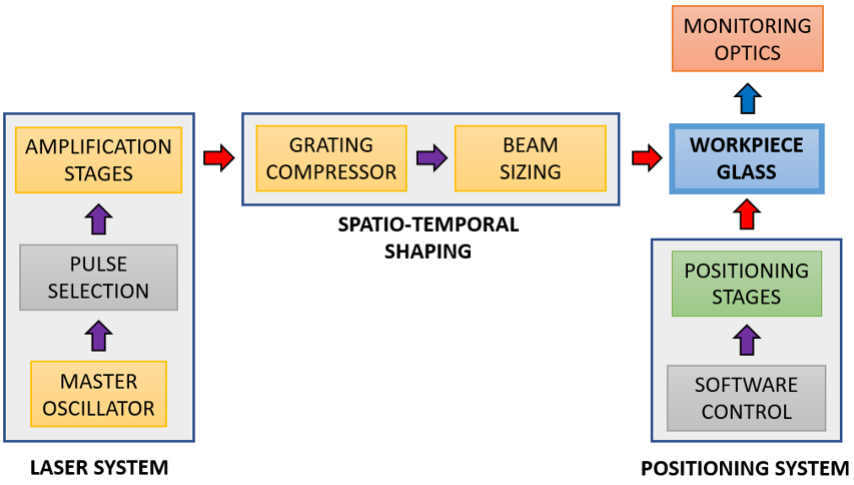


Figure 5.1: Block diagram of the direct-write bench system.

After amplification and compression, the signal was routed to the fiber workpiece. A shutter was used in the beam path between the grating compressor and the focusing objective to block the beam during the translation between individual line writes, which allowed for the write characteristics to be fully customizable in addition to decoupling the write pattern from any thermal effects in the fiber that would arise from constant exposure to the signal. The fiber had full linear 3-axis positionability with precision down to 30 nm that was fully automated via a LabVIEW virtual instrument that was written in-house that integrated a number of manufacturer supplied instrument drivers. A manual 2-axis angular positioning stage was placed on top of the automated linear stage setup for the user to be able to align the fiber axis such that it maintained the proper focus position across the extent of the write. The third angular axis (rotation along the fiber transmission axis) was unnecessary, as the setup was

only configured to process non-polarization maintaining fiber. The workpiece holder is mounted on top of the angular positioning stage; the fiber is clamped so it sits on a microscope slide that features LED illumination from below.

The focusing objective was a 1.25 NA, 100x oil immersion lens that was dipped in index matching fluid for fused silica. The objective allowed for a sub-micron spot radius at 1030 nm, and the matching fluid was used to mitigate any aberrations that would be induced by propagating the write signal through the curved fiber-air interface. The objective was also used as part of an imaging system for the purpose of proper fiber positioning and inspection. This optical system has a portion of its optical path that is different than the write laser path, and thus their focus positions are different. The bottom illumination serves the imaging system.

Figure 5.2: Workpiece holder used for grating fabrication.

The write pattern used for the gratings fabricated for this report is shown in Figure 5.3. Lines were chosen over points because they are less sensitive to alignment and cover more of the fiber core, which enhances the reflective magnitude of the grating structure. In addition, line structures are much faster to fabricate than plane structures and do not have the same difficulties with constantly changing focus characteristics. The blue lines represent the positioning procedure movements (when the laser shutter is closed) and the red lines represent movements where index modification lines were being written (when the laser shutter is open). The pattern that was used features writing in only a single direction, as it was found that this procedure produced more uniform results. The system had the option of setting separate speeds for positioning and writing movements because they serve different but equally important functions: positioning needed to be slow enough so as not to impact stage precision, and line writes needed to be fast enough so as not to damage the fiber. In the end, the values were set equal for this experiment and those produced acceptable results, but that was not something that could be assumed a priori.

Proper start positioning was accomplished using a rudimentary image processing program written in MATLAB. Per the advice given in a technical document published by Newport Corporation [16], the fibers were positioned so that

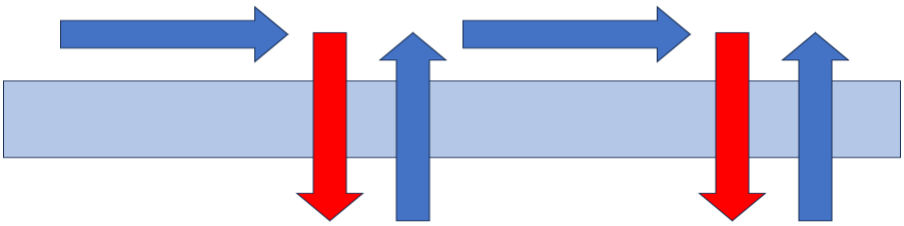

Figure 5.3: Write pattern used for grating fabrication.

the core-cladding boundary disappeared: this is the criteria for a fiber being in focus. In practice, this is a difficult discernment to make with the naked eye; focus offsets of 10 microns below or above the center position point all appear nearly the same. As a result, alignments using just the eye often yield grating structures that are written outside the core, and thus show no reflection band. However, their differences become much more obvious upon processing, and the fiber can be placed appropriately when the operator uses this tool as a feedback mechanism.

Once the focus position is found, some sacrificial writes needed to be performed to determine the laser focus position offset from the fiber focus position. This offset calibration only needs to be performed once as long as the lens elements (for collimating/focusing) in the system are not moved in a drastic way. The image processing program increased the positioning fidelity such that nearly all test writes performed after its implementation featured modifications that were in the core. This was verified via imaging and via the existence of a reflection band.

It should be noted that the write signal repetition rate of 1 MHz is decidedly high for direct-write processes. For the experiment described in this document, operation at 1 MHz was necessary, as there was an effort to utilize the materials that were readily available to get the development process started. Much of the literature features write signals with much lower repetition rates (10 kHz and below) [16][17][18]; however, there is research that supports the idea of using multiple write passes to mitigate the variance of write signal behavior with promising results [19], implying there is some benefit to a higher exposure fluence in write locations. The method used for the experiment described in this report (this document, not the reference) did not feature multiple write passes, but it did feature a high number of pulses per line (about 400,000 over a 40 micron distance), so there was a higher total fluence and a likely 'smoothing out' of pulse fluctuations. More research needs to be done to confirm if a high fluence signal is actually beneficial for a single-pass write routine.

The spectral properties of the fabricated gratings were characterized using a Hewlett-Packard 86142A optical spectrum analyzer. The test signal came from the 10% port of a 90:10 coupler spliced to the output of the master oscillator

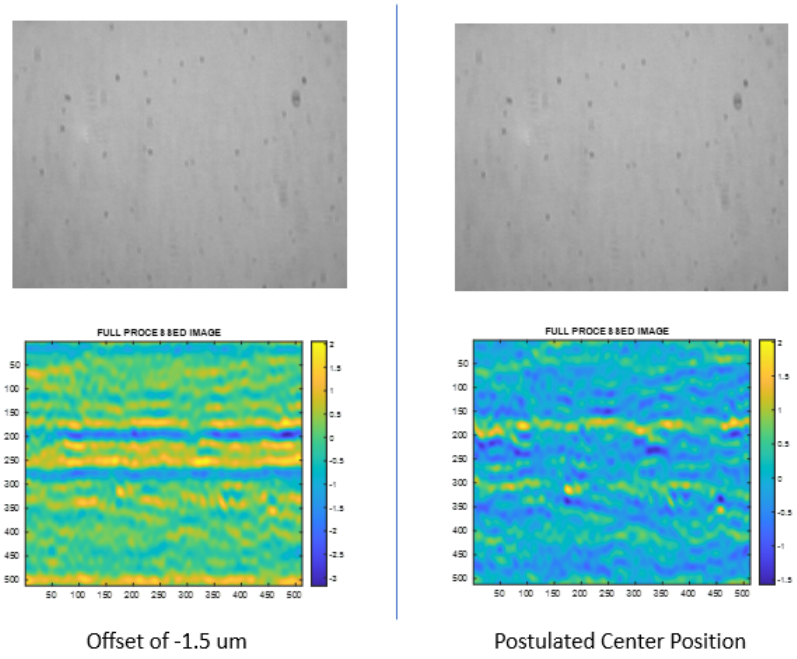


Figure 5.4: Comparison of a fiber that is in focus and a fiber that is 1.5 microns out of focus in unprocessed (top row) and processed (bottom row) formats. Note that the top pictures are nearly identical.

that was generating the writing signal (Menlo Systems Blue Cut OEM Seed). Note that the signal of the 90% arm routed the signal to the amplifier chain to be boosted before interacting with the workpiece fiber. The test signal arm was spliced to a four-port fiber circulator at PORT1. Fabricated fiber Bragg gratings under test were spliced to the PORT2 arm, and the test signal output at PORT3 was put into the optical spectrum analyzer for reflectance spectrum evaluation. The remaining circulator port (PORT4) remained unused.

The test setup was calibrated by splicing a flat FC/PC fiber connector to the output of PORT2 and recording the resulting reflectance spectrum. This spectrum corresponded to about 4% reflection at each of the wavelengths for which there was signal; a silica-to-air flat interface has roughly this magnitude of reflection per the Fresnel equations [8]. The setup had a usable evaluation range between about 1020 nm and 1050 nm; outside of this window, the test signal did not have sufficient power to separate itself from the intrinsic noise of the optical spectrum analyzer. The calibration spectrum is shown below in Figure 5.6.

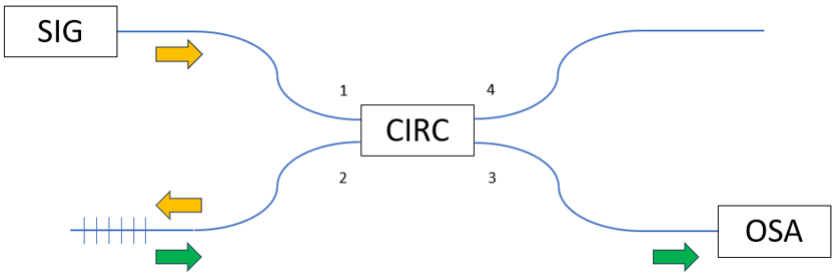


Figure 5.5: Circuit diagram of the grating test setup.

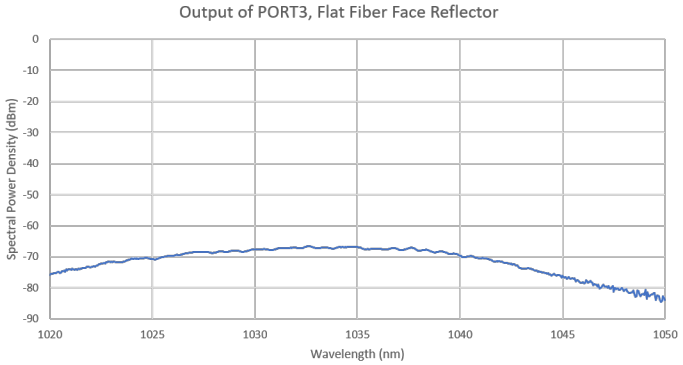


Figure 5.6: Test calibration spectrum used for grating characterization.

## 5.2 A Description of Basic Experiments

There were many basic experiments performed for the development of the grating fabrication process. Many of these experiments were qualitative in nature, as this endeavor was entirely new to the parties involved and empirical knowledge that is clear now was not so clear at the outset of this project. Some experiments had clear results, such as the determination of the proper write pattern, but others happened over the course of months. The result of most of this work cannot be quantified, it can only be described.

Extensive experiments were performed to determine the optimal way to find the absolute fiber position relative to the focusing objective, as this is perhaps the most important positioning parameter for successful grating writes. In early iterations of the process, the positioning was done by hand with the positioning stage that the microscope objective was pinned to. This method was appropriate for a double-clad fiber that was initially in use; however, once single-mode fiber was being used for the writes, it became much more difficult to align by hand. An attempt to use the z-positioning stage for fine alignment was employed because it was believed that the write inconsistencies were from human error.

This turned out not to be the case, as the problems with being unable to write in the core consistently continued. As described in the previous section, the problem was the inability to discern what focus looked like on the inspection camera.

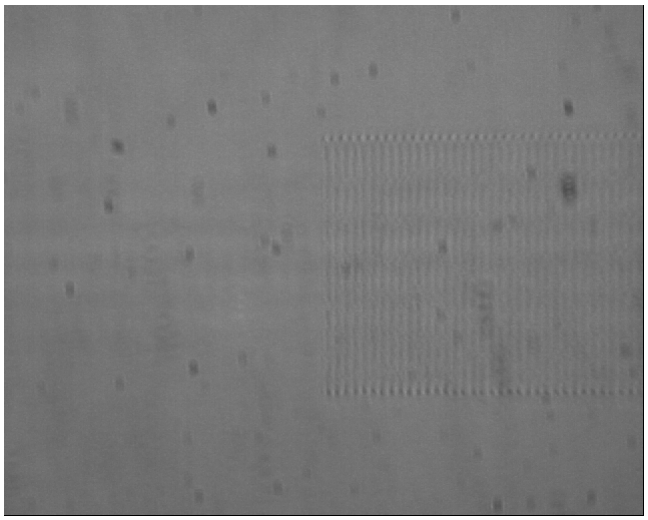

Figure 5.7: Image of a grating structure in focus with a fiber core out of focus, indicative of the grating structure being written outside the core.

The image processing routine that was described in the previous section was the terminal method (as far as this report goes) used for alignment. This method is still manual as it requires the user to operate the z-positioning stage, so there is still opportunity for improvement. However, to this point, it has shown consistent results.

Determination of usable pulse energies was a layered problem. Initially, it seemed that the pulse energies that were used had too little energy, as there was very inconsistent reflection behavior from write to write. To remedy this, the energy was increased to attempt to increase the maximum value of the reflectivity. This was met with mixed results, as there was once again lots of variability between subsequent writes. However, the images taken of the inscribed lines were very easily visible and looked more uniform. This was initially interpreted as a positive result.

As the energy experiments happened in tandem with the alignment experiments, the pulse energy variation data could always be questioned because of alignment inconsistencies. Once the alignment process was set in order, writes with high pulse energies still continued to show variable results. It wasn't until the pulse energy was dropped again and began to show more promising results that it was realized that the strong line contrast was actually indicative of damage.

Figure 5.9 is a picture of single-shot damage spots. The character of these

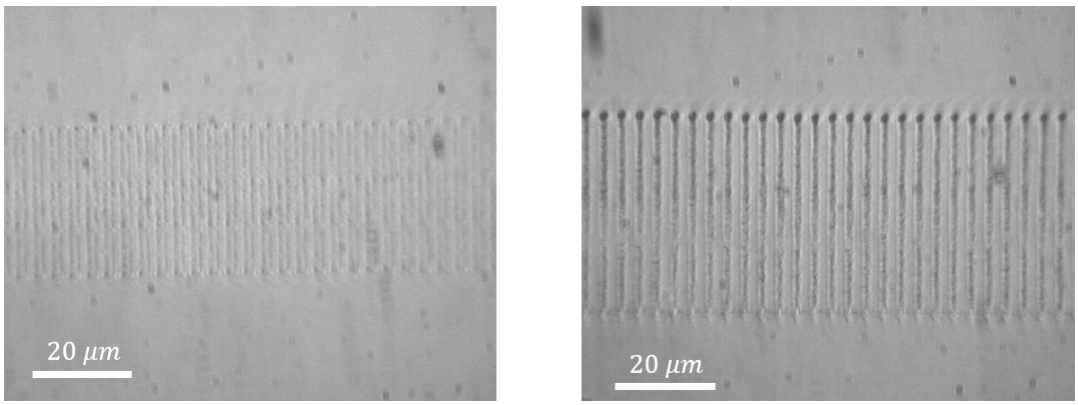


Figure 5.8: Example of low energy dosage line writes (left) versus high energy dosage line writes (right).

spots was not initially obvious because the high pulse energy signals were only being used to write lines before the time of the picture. The side view makes the damage clear. It was determined that energies around 175 nJ at the compressor output (about 120 nJ at the workpiece) were appropriate for damage-free writes. This number is in the neighborhood of the energies reported in References [17] and [18].

One of the most important basic experiments conducted concerned the width of the lines that were being written. As the equations in the Coupled-Mode Analysis section of the previous chapter imply, grating visibility is an important factor for increasing the magnitude of reflectivity of grating structures. Considerations for write parameters were made to result in a structure that had high index contrast between the modified and unmodified sections of the fiber; the desired outcome was a visibility of one. However, care was taken to choose a longitudinal periodicity that was not so large that the modifications deviated too much from a sinusoidal character, a form that was desired for the early development stage of the fabrication process to streamline analysis. Ultimately, it was determined by inspection that the spot size was approximately 1.4 microns, so the minimum grating periodicity was twice that amount, about 2.8 microns.

The results of these basic experiments performed early on was crucial for the later stages of the project.

## 5.3 Preliminary Mathematical Modeling

Modeling software was developed in-house on the MATLAB platform, which has all of the necessary functionality to produce results quickly with the help of the native functions. In reality, this analysis was done in large part with analytical results, so the only necessary capability was efficient evaluation of hyperbolic

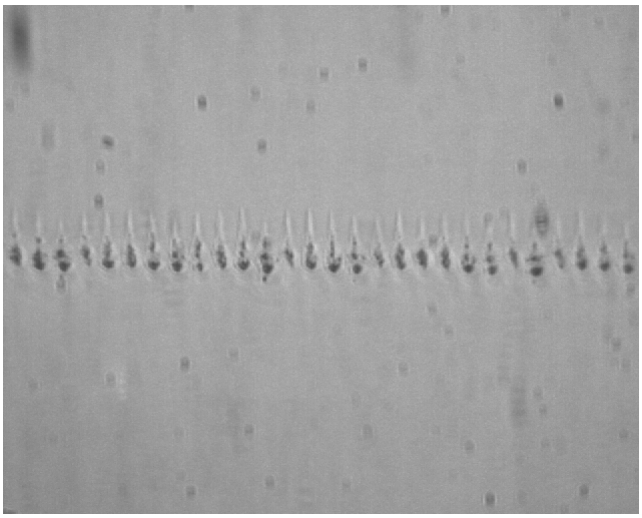

Figure 5.9: Example of damaged spots from use of excessive pulse energy.

trigonometric functions and Bessel functions. The only exception was the need for a nonlinear root finding routine to calculate the bV-curve.

The properties of the fiber were the only modeling results that were necessary to begin the experiment; knowledge of the dispersion function was required in order to set the grating periodicity. The fibers that were used for the experiment were two sections of Newport F-SMF-28 fiber (equivalent to the industry standard SMF-28 fiber). This fiber has the following properties [5]:

- The core diameter value is 8.2 microns
- The cladding diameter value is 125 microns
- The numerical aperture value is 0.14
- The core is made of a silica host doped with a small concentration of germanium oxide
- The cladding is made of pure silica

Given the value of the core diameter, the numerical aperture, and the assumption about the cladding material, it is possible to estimate the value of the fiber dispersion at each of the wavelengths of interest, and consequently the shape of the mode field at each of those wavelengths. The dispersion curve for the fiber in the spectral region of interest was calculated to have the form shown in Figure 5.10.

Of note, the fiber being used for this experiment is multimode, as it guides the fundamental mode ($LP_{01}$) and the $LP_{11}$ mode. The $LP_{11}$ mode was not considered for the analysis in this report as it is relatively weakly confined in

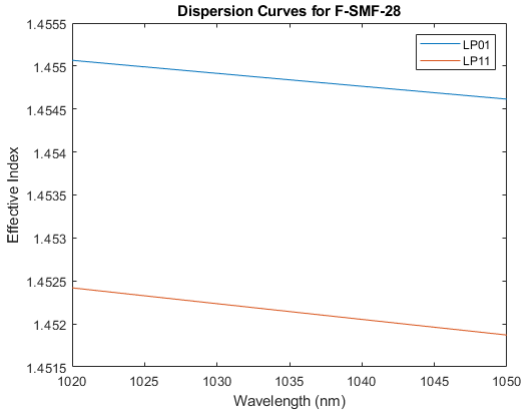


Figure 5.10: Dispersion curves of Newport F-SMF-28 fiber based on datasheet values near 1030 nm.

the fiber; however, the full explanation for some of the behaviors exhibited in the experimental data require the consideration of this mode.

The coupled-mode equations described in the previous section were implemented in software with some assumptions made about the system, the biggest of which was that the index modification function was constant in the transverse direction. This assumption was made because the index modifications were planned to be lines and thus were to cover the extent of the core in one dimension. Initial basic experiments showed that the depths of the modifications were larger than the period length of the gratings, which were just over 2.8 um.

Figure 5.11 was one of the first images taken of a side view of one of the index modification spots. Too much energy was used to write the spot, but it is obvious that the modification has a depth greater than the period. Equations 4.7 and 4.8 state that the coupling behavior of the forward- and backward-propagating waves is dependent on the overlap of the mode field and the transverse profile of the index modifications. If there is sufficient overlap between these two functions in their highest-value regions, the value of the product of the mode field with the actual transverse modification function would approximate the product of the mode field with a theoretically constant transverse modification function. Figure 5.12 compares the functional form of the fundamental mode field and a functional form of a line modification with a depth of 4 microns.

By inspection, it seems that the transverse modification function above fits the constant function approximation criteria, although this was not explicitly calculated.

Using the coupled-mode equations with some values for the index modification depth found in literature under similar experimental conditions (values of $\delta n$ between $3\times10^{-4}$ and $1\times10^{-3}$) [2][16][20], it was determined that grating lengths between 0.1 and 0.5 mm gave a wide variety of potential grating characteristics with marked differences from each other. As such, this was to be the

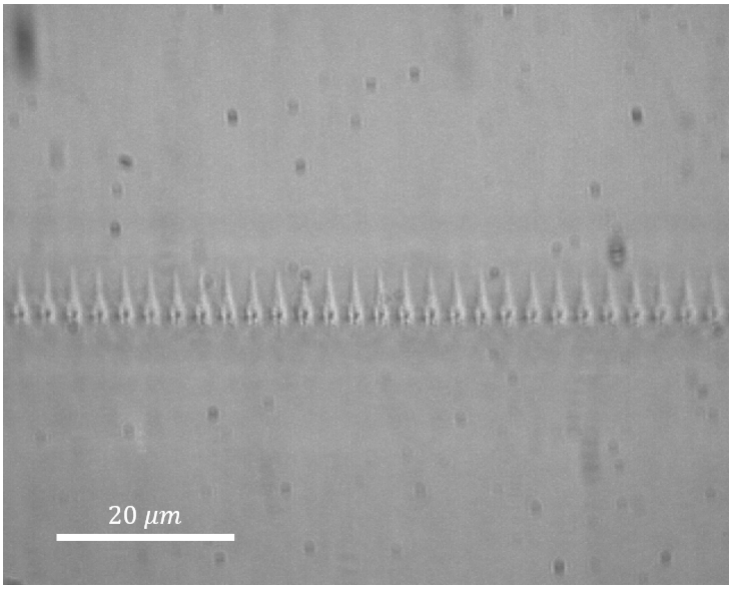


Figure 5.11: Teardrop-shaped index modifications imaged from the side; the period is 2.8 microns.

region of interest for the first gratings that were to be written with the first fully functional iteration of the system. Note here that $\delta n$ refers to the total prominence of the index change (the full index change) over the index of the unchanged substrate, whereas the value $\Delta n$ refers to the sinusoidal amplitude value of the index change function in the coupled-mode analysis.

## 5.4 Initial Experiment Results and Model Calibration

The first step of the experimental effort was calibration of the model parameters; in particular, the value of the amplitude of the index modification function needed to be determined for the system that was being developed, as it exhibited different characteristics than any of the systems in the pool of literature that was explored.

It was decided that the best route to initial calibration was to write two gratings at the same pulse energy and write speeds, but with different lengths. Upon testing, this dataset would allow for two verifications of the magnitude of the index change at the specified pulse energy under different circumstances. The first grating was to have a high reflectivity value, as it would prove that the system was functioning in an obvious way with a sharp feature that was prominent above any noise present in the test setup. Naturally, this meant that

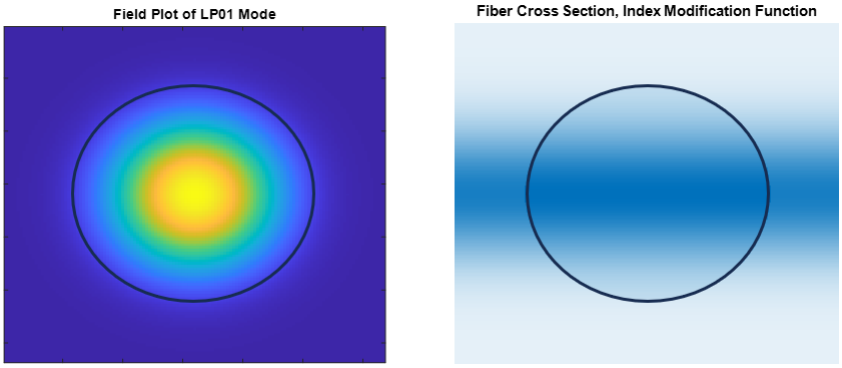


Figure 5.12: Comparison of the $LP_{01}$ intensity profile with a Gaussian transverse index modification function with a FWHM depth of 4 microns; the black circles represent the fiber core boundary.

this grating would have a relatively long longitudinal extent–early simulations suggested that 400 microns was sufficient to see peak reflectivity behavior well above 50%. The second grating was to have a larger bandwidth than the first grating; this meant that it would likely have a lower peak reflectivity. Simulations showed that a grating region length of 100 microns would produce a larger bandwidth under the same assumed magnitude of the index modification while still maintaining a reflectivity of greater than 10%, discernible above any reflections off of flat fiber faces in the system.

These gratings were written with a period of 2.86 microns, which corresponds to a 8th-order grating centered around 1035 nm for the lowest order mode in the fiber. The length of the lines written for these devices was selected to ensure that the entire extent of the core was exposed to the write signal, as the line length was almost five times that of the core diameter. Positioning and writing speeds were chosen to allow for the fastest possible fabrication speed without sacrificing quality. Finally, the pulse energy used was empirically shown to produce uniform, repeatable index modifications.

The first grating was named "SCRIBE055". Some of its properties have already been stated but will be restated here so the information is all in one place:

- The grating period is 2.86 microns
- A grating region length of 400 microns
- Transverse line lengths of 40 microns
- A positioning speed of 100 microns/second
- A line write speed of 100 microns/second

- A pulse energy of about 175 nJ at the compressor output, with a pulse energy of about 120 nJ at the workpiece

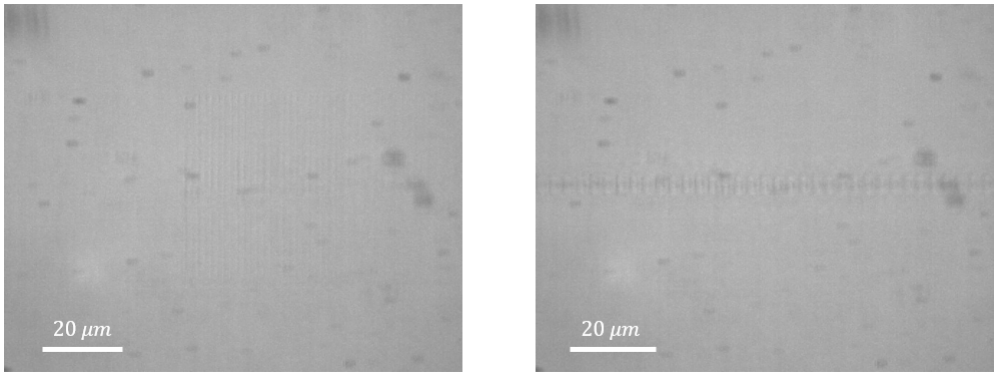


Figure 5.13: Write view (left) and side view (right) of SCRIBE055.

SCRIBE055 shows excellent line shape and index modification uniformity; the side views shows pill-like line profiles that appear to be almost exactly replicated throughout the whole structure. The reflection characteristics of SCRIBE055 are shown in Figure 5.14.

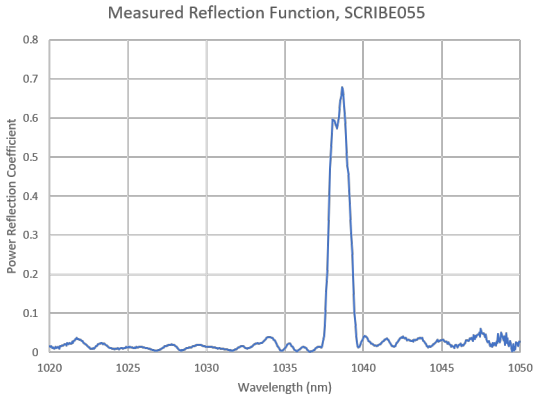


Figure 5.14: Reflection spectrum for grating SCRIBE055.

The reflection spectrum shows the high reflectivity behavior that was sought; the peak value of which approaches 70%. The center wavelength is at about 1039 nm with a bandwidth of about 2 nm. This result is certainly promising, as the demonstration of a high value reflector speaks to the general effectiveness of the process.

The second grating was named "SCRIBE056". It has the following properties:

- The grating period is 2.86 microns
- A grating region length of 100 microns
- Transverse line lengths of 40 microns
- A positioning speed of 100 microns/second
- A line write speed of 100 microns/second
- A pulse energy of about 175 nJ at the compressor output, with a pulse energy of about 120 nJ at the workpiece

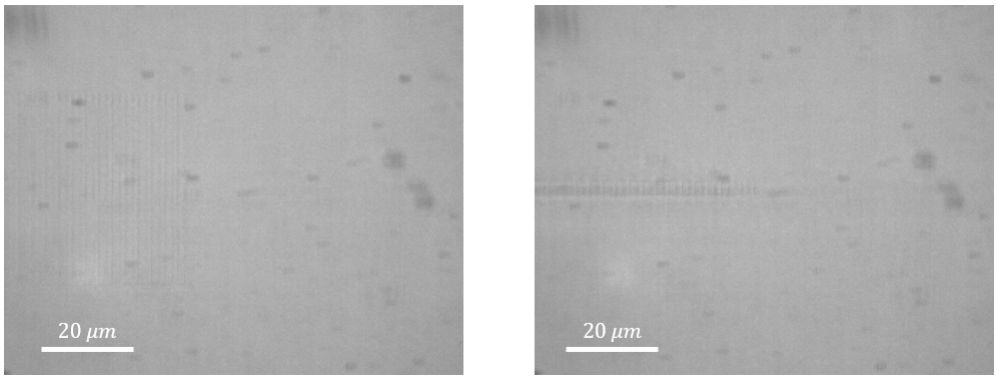


Figure 5.15: Write view (left) and side view (right) of SCRIBE056.

SCRIBE056 shows the same uniformity in the write plane that SCRIBE055 does, however, the side view does not feature the line profiles as profiles as clear. This is likely just an imaging artifact, and the repeatability from line to line still appears strong. The center wavelength is at about 1039 nm with a bandwidth of about 4 nm.The reflection characteristics of SCRIBE056 are shown in Figure 5.16.

It is obvious that the bandwidth has increased; it appears to be around twice as large as the bandwidth exhibited by SCRIBE055. The peak reflectivity was also heavily decreased to a value of just above 10% as was expected. In addition, there are spike-like spectral features in the spectrum; it is unclear why these features arose. It is possible that there is interference between the signal reflected from the grating structure and other parasitic signals that may have originated via reflection off of splices, etc. Further testing has to take place to verify this claim.

For the model calibration, an index modification value had to be chosen that reflected agreement for both of the gratings that were written: ideally, since the

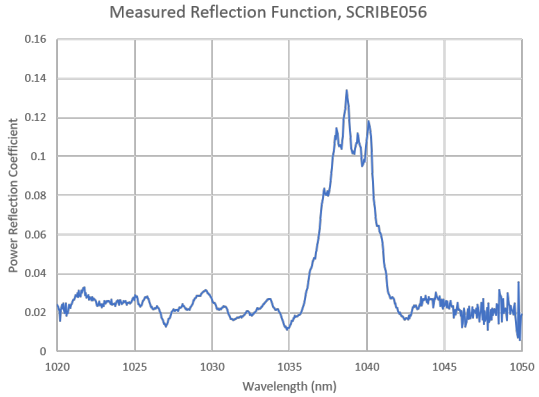


Figure 5.16: Reflection spectrum for grating SCRIBE056.

same write speed and write energy was used, this value should have been the same for both devices. After some consideration, it was determined that a value of $\delta n \approx 5.4 \times 10^{-4}$ ($\delta n$ represents the total index change, not the average index change that $\Delta n$ represents) was the most representative of the change that took place. This value overshoots the peak value of SCRIBE055 and undershoots the peak value of SCRIBE056. It should be noted that this estimate was arrived at solely by inspection; numerical calculation of this result requires an analysis of the proper data filtering procedure that has yet to be performed at the time of the writing of this report.

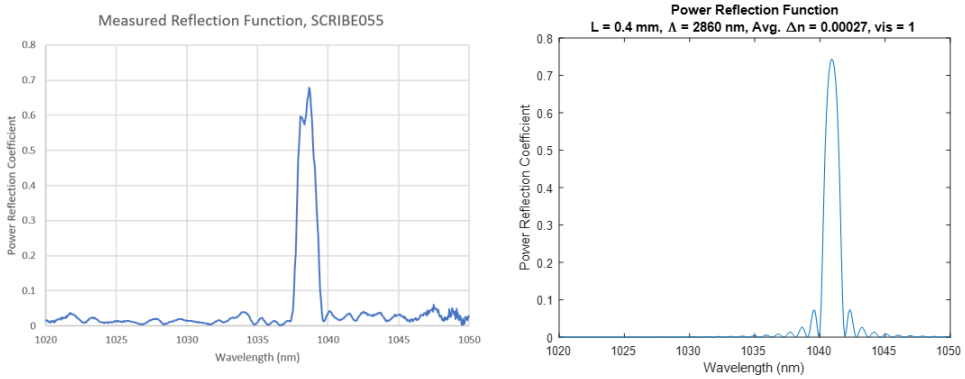


Figure 5.17: Comparison between experimental results (left) and modeling results (right) for SCRIBE055.

The modeling results and the experimental results show excellent agreement with regards to bandwidth, with both devices showing almost exactly the band

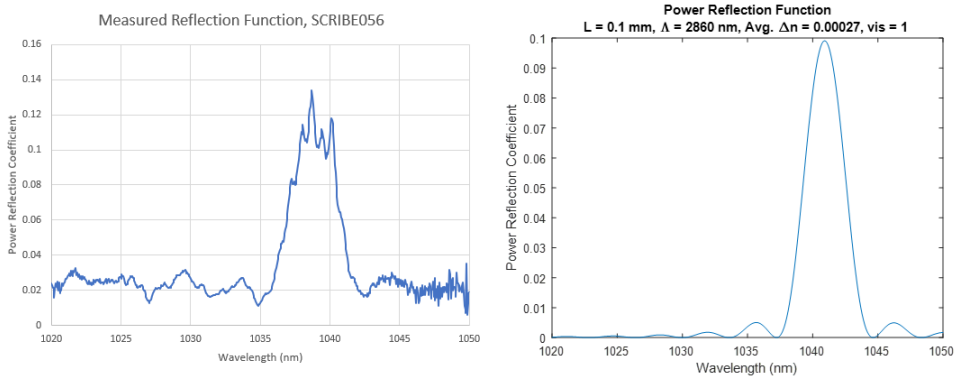


Figure 5.18: Comparison between experimental results (left) and modeling results (right) for SCRIBE056.

extents that were predicted by the model.

The center wavelength behavior was not equivalent in the model and experiment. There are a number of reasons that this could have occurred, but the likely reason is just positioning stage inaccuracy. As Figure 4.2 shows, even deviations from the phase matching condition on the order of one to five parts in one thousand can manifest as changes of center wavelength changes of many nanometers near a signal wavelength of 1 micron. An additional source of error could be strain induced in the fiber during the mounting process.

## 5.5 Secondary Experiment Results

For the write of the third grating, the goal was to maintain the wide-band behavior that SCRIBE056 exhibited while increasing the magnitude of the reflection. A device with these characteristics would support a larger bandwidth when placed into a fiber master oscillator, which would mean that the device could support shorter compressed pulse durations, a feature that is important for these devices.

The method chosen to increase the reflectivity and maintain the bandwidth was to increase the index modification value, which was made possible by increasing the pulse energy. As stated earlier in this report, the process by which refractive index is modified by ultrashort pulses is highly nonlinear, and as such, a small increase in the pulse energy should yield comparatively large changes in the induced index change. For this experiment, the energy was increased by just over 10%, which would increase the induced index change by around a factor of two for the theorized eight-photon process that takes place for a 1030 nm write signal.

The third grating is named "SCRIBE057". It has the following properties:

- The grating period is 2.86 microns

- A grating region length of 100 microns
- Transverse line lengths of 40 microns
- A positioning speed of 100 microns/second
- A line write speed of 100 microns/second
- A pulse energy of about 200 nJ at the compressor output, with a pulse energy of about 135 nJ at the workpiece

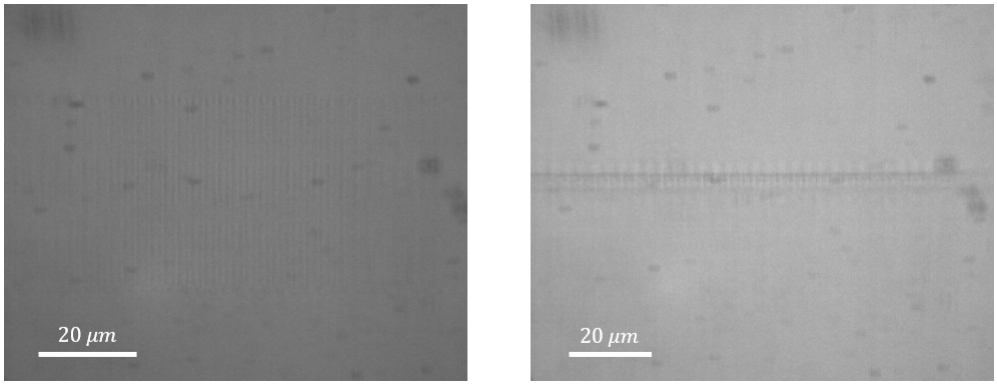


Figure 5.19: Write view (left) and side view (right) of SCRIBE057.

The increase in energy did not have an adverse effect on the line structures; they still appeared uniform and clean. SCRIBE057 looks very similar to SCRIBE056. The center wavelength is at about 1039.5 nm with a bandwidth of just under 4 nm. The reflection characteristics of SCRIBE057 are shown in Figure 5.20.

This device exhibits comparable bandwidth to SCRIBE056 but with nearly three times the value of the peak reflectivity. There are discernible sidebands in this spectrum as well, a feature that is expected due to a short grating length. These artifacts were not obviously present in the reflection spectrum of SCRIBE056 because they had amplitudes that were below the noise floor of the testing setup. There is also less spiking behavior present in the spectrum.

The value of the index modification value chosen to fit the modeling and experimental data was $\delta n \approx 1 \times 10^{-3}$. With this value, there is excellent agreement between the bandwidth and the peak reflectivity, and the shape is nearly the same save for a small spike in the reflection spectrum. There is still the center wavelength offset that was present in the modeling and experimental results for SCRIBE055 and SCRIBE056, probably for the same reasons. It should be noted that according to some literature [2], this value is approaching the upper bound of the isotropic index changes; though some other sources suggest this value is well below it [20].

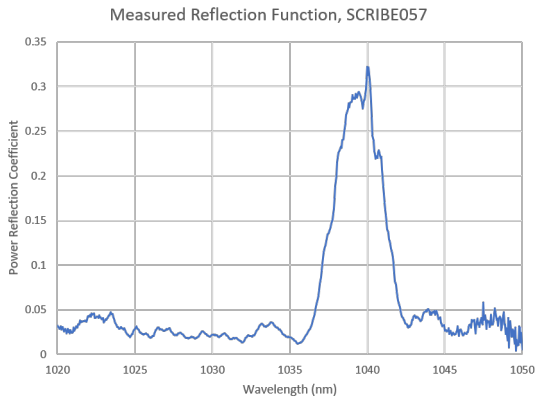


Figure 5.20: Reflection spectrum for grating SCRIBE057.

The induced index change was a factor of 1.85 times greater than the estimated change for SCRIBE055 and SCRIBE056, which is below the 2.14-2.57 that is predicted for an energy increase of 10-12.5%. The lower than expected result could be attributed to the fact that the compressor was not adjusted upon the energy change; thus, any pulse dynamics that arose as a result of the higher system pulse energy may have remained uncorrected, leaving the pulse with a peak power that did not scale in the same way the energy did. In reality, there are a number of reasons that these numbers did not align perfectly, everything from instrument precision to the characteristics of the workpiece fiber. Considering the breadth of sources of deviation from the ideal, the results that were demonstrated are actually fairly consistent with theory.

## 5.6 Additional Comments on Experiment

Due to the success of SCRIBE057, another write was performed where the pulse energy was increased to a value of about 225 nJ at the compressor output in an attempt to scale the index modification value further. However, the resulting device did not have the higher reflectivity that would have been consummate with an increasing index modification value. It is possible that at this energy, the modifications took on a different character; values of the index modification greater than that which was assumed in this report approach regimes where nanogratings are formed in the modified locations ($\delta n > 3{\times}10^{-3}$), and greater values than that imply the formation of microvoids in the fiber ($\delta n{\approx}1{\times}10^{-1}$) [2]. It is possible that the experimental conditions did not support these structural changes; the signal average power may have been too high at this point to form clean nanogratings or voids in the exposed spots.

In general, there was only a small portion of the energy bandwidth that could be used to modify the fiber without damaging it. While the system was

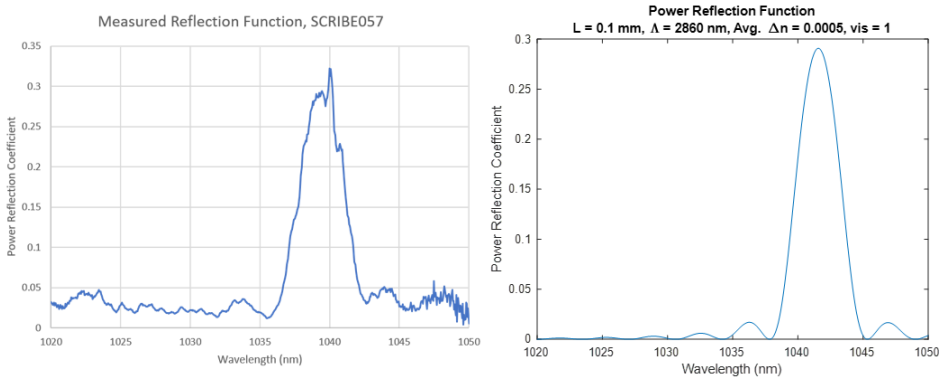


Figure 5.21: Comparison between experimental results (left) and modeling results (right) for SCRIBE057.

capable of delivering 1 uJ pulses of clean (in-band) energy, fibers exhibited slight damage when exposed to pulse energies of about 250 nJ, and heavy damage at energies greater than 400 nJ. These numbers were lower than anticipated, based on some of the energies that were reported as being used in literature [16].

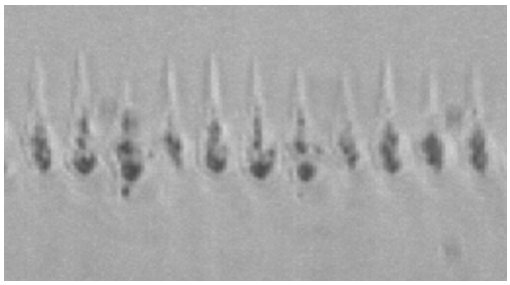

Figure 5.22: Zoomed in image of damaged spots, note the raindrop tails above the damage.

The shape of the damaged fibers was interesting, as the spots turned from ellipsoid-like shapes that were nearly symmetric along the path of propagation for the write laser (which is perpendicular to the fiber direction of travel axis) to raindrop-shaped modifications. One theory as to why this happened [21] is that since the index modifications are believed to be the result of a nonlinear process, beams with excess energy met the energy condition to modify the material earlier in their propagation through the workpiece, and thus began doing so. The reason that this modification was not symmetric may be due to attenuation of the beam by the time it passed through the focus, rendering the signal with insufficient energy to modify the workpiece on the other side of the focus. The slender feature on the 'source side' of the modification could possibly be

explained by the center of the beam meeting the condition sooner; the increase in the size of the feature closer to the focus is consistent with this theory.

To be able to truly correlate experiment with modeling, measurements of refractive index profiles need to be developed. Since images of the refractive index modifications are possible with the monitoring system, accurate estimations of the grating thickness in the transverse dimensions can be made. Thus, a model of the diffractive behavior of a planar grating structure written in glass can be used to back-calculate the magnitude of the index modification given diffraction angles and signal power in some of the diffracted signal orders. This method is described in Reference [22]. To apply this method, the use of fibers is not necessarily required; if the fiber in question is made of a material for which bulk substrate is available for purchase, a larger planar structure can be written into the substrate and characterized as a thin volume grating to calculate the values of interest. This method should return the first-order characteristics of the grating structures, but more detailed information will still be absent. A phase-based tomography method for index characterization also exists [23]. This method and others like it are more mathematically involved but give a greater insight into the spatial characteristics of the index modifications. A series of sinograms are captured at different positions along the fiber transmission axis and processed to construct the cross-sectional index profile at each position; the cross-sections are then stitched together to produce a three-dimensional rendering of the refractive index profile of the fiber. This method is limited by the imaging resolution of the setup and the dynamic range of the index modifications that can be measured; these seem to be only challenges that can be remedied with better engineering but this claim has not been explored at the time of the writing of this document.

Once the refractive index profile has been more accurately measured, the modeling procedure can be matured accordingly. Resolving the index modification function allows for a more accurate calculation of the coupling coefficients for coupled-mode analysis, which are based entirely on the transverse expression of the index modifications. The coupling rate over the device can thus be more accurately determined. Also, a more robust expression of the longitudinal variation of the index modification function can be decomposed into its spectral components to take into account the effect that structure that is not phase-synchronous has on the reflection behavior. The Coupled-Wave Equations can be solved for each spectral component and their resulting reflection coefficients can be summed at each wavelength under test to return the system aggregate behavior. The result may better describe more complex behavior such as the structure of the out-of-band reflection. Additionally, a fully resolved index modification function also enables the use of fully numerical modeling techniques, like the use of Rouard's Method mentioned earlier in this document. Fully numerical techniques allow for resolution of finer features in the reflection function, the knowledge of which can be very important for certain applications.

As far as general system improvements go, a full fine-tuning of the setup from an optical and mechanical engineering perspective would likely go a long way to improve the process yield. Stability of the write laser to the greatest degree

possible is a must; this can be accomplished by making it entirely in-fiber until it is compressed in free space. Increasing the stability of all of the opto-mechanical beam-routing components and the of the workpiece positioning components by isolating them from mechanical vibrations and air currents will also improve yield [21]. These considerations will lead to non-negligible improvements–for example, one system change reduced the beam path by more than 65 percent, which reduced the RMS beam wander in a significant way. From a design perspective, the system still needs to be analyzed and configured so that the beam is of the proper size when it reaches the entrance pupil of the microscope objective, which will allow for the smallest possible write laser spot.

Finally, these devices still need to be placed into fiber master oscillator systems to determine if they can fulfill the original task of the project–the selection of the center wavelength of said master oscillator devices. This will be the ultimate test of the success of the project and is a focus of the near-term future of this effort.

# Chapter 6

# Conclusion

The degree to which the methods described in this document actually functioned to produce gratings that are potentially fieldable was surprising. The breadth of available modeling procedures allows the user to decide how detailed they wish to get in their analysis, with meaningful results being available to the interested party with even small levels of time investment. The experimental setup features components that are all readily available for purchase from nearly every large vendor of products for optical physics laboratories. Many of the components are likely already in the laboratory and only need slight reconfiguration to function as useful parts of a grating manufacturing station. While the initial goal of the project to this point has still not been fulfilled, the project is still ongoing and the results presented in this report are promising. If the reader has the need for custom fiber Bragg gratings, especially those with constantly evolving or novel characteristics that are used in research, they should strongly consider the use of a direct-write process for the fabrication of their devices in-house.

# Chapter 7

# References

(1) K. M. Davis, K. Miura, N. Sugimoto, and K. Hirao, "Writing waveguides in glass with a femtosecond laser," *Optics Letters*, vol. 21, no. 21, p. 1729, Nov. 1996, doi: https://doi.org/10.1364/ol.21.001729.

(2) J. Thomas, C. Voigtländer, R. G. Becker, D. Richter, A. Tünnermann, and S. Nolte, "Femtosecond pulse written fiber gratings: a new avenue to integrated fiber technology," *Laser & Photonics Reviews*, vol. 6, no. 6, pp. 709–723, Feb. 2012, doi: https://doi.org/10.1002/lpor.201100033.

(3) A. Zoubir, M. Richardson, L. Canioni, A. Brocas, and L. Sarger, "Optical properties of infrared femtosecond laser-modified fused silica and application to waveguide fabrication," *Journal of the Optical Society of America B*, vol. 22, no. 10, p. 2138, Oct. 2005, doi: https://doi.org/10.1364/josab.22.002138.

(4) K. Itoh, W. Watanabe, S. Nolte, and C. B. Schaffer, "Ultrafast Processes for Bulk Modification of Transparent Materials," *MRS Bulletin*, vol. 31, no. 8, pp. 620–625, Aug. 2006, doi: https://doi.org/10.1557/mrs2006.159.

(5) "F-SMF-28 Optical Fiber," *www.newport.com.* https://www.newport.com/p/F-SMF-28

(6) B. E. A. Saleh and M. C. Teich, *Fundamentals of Photonics.* Hoboken: Wiley, 2019.

(7) J. Bures, *Guided optics: Optical Fibers and All-Fiber Components.* Weinheim: Wiley-Vch, 2009.

(8) C.-L. Chen, *Foundations for Guided-Wave Optics.* John Wiley & Sons, 2006.

(9) E. Snitzer, "Cylindrical Dielectric Waveguide Modes*," *Journal of the Optical Society of America*, vol. 51, no. 5, pp. 491–491, May 1961, doi: https://doi.org/10.1364/josa.51.000491.

(10) D. Gloge, "Weakly Guiding Fibers," *Applied Optics*, vol. 10, no. 10, p. 2252, Oct. 1971, doi: https://doi.org/10.1364/ao.10.002252.

(11) E. Kudeki, "Optical Fibers -supplementary notes." Nov. 24, 2012. Accessed: May 06, 2024. [Online]. Available: https://courses.engr.illinois.edu/ece350/OpticalFiberNotes_Kudeki.pdf

(12) R. Kashyap, *Fiber Bragg Gratings*. San Diego: Academic Press, 1999.

(13) A. W. Snyder, "Continuous Mode Spectrum of a Circular Dielectric Rod," *IEEE transactions on microwave theory and techniques*, vol. 19, no. 8, pp. 720–727, Aug. 1971, doi: https://doi.org/10.1109/tmtt.1971.1127613.

(14) R. K. Kostuk, *Holography*. CRC Press, 2019.

(15) L. A. Weller-Brophy and D. G. Hall, "Analysis of waveguide gratings: application of Rouard's method," *Journal of the Optical Society of America A*, vol. 2, no. 6, pp. 863–863, Jun. 1985, doi: https://doi.org/10.1364/josaa.2.000863.

(16) "A versatile machine optimized for the fabrication of Fiber Bragg Gratings (FBGs) by femtosecond laser direct-writing." 2019. Accessed: May 06, 2024. [Online]. Available: https://www.newport.com/medias/sys_master/images/images/hed/heb/9363754549278/DS-011702-App-Note-61-0919.pdf

(17) A. S. Chernikov, K. S. Khorkov, D. A. Kochuev, R. V. Chkalov, V. G. Prokoshev, and N. N. Davydov, "Line-by-line fiber Bragg grating fabrication by femtosecond laser radiation," *Journal of Physics: Conference Series*, vol. 1164, p. 012015, Feb. 2019, doi: https://doi.org/10.1088/1742-6596/1164/1/012015.

(18) K. Zhou, M. Dubov, C. Mou, L. Zhang, V. K. Mezentsev, and I. Bennion, "Line-by-Line Fiber Bragg Grating Made by Femtosecond Laser," *IEEE Photonics Technology Letters*, vol. 22, no. 16, pp. 1190–1192, Aug. 2010, doi: https://doi.org/10.1109/lpt.2010.2050877.

(19) D. V. Przhiialkovskii and O. V. Butov, "High-precision point-by-point fiber Bragg grating inscription," *Results in Physics*, vol. 30, p. 104902, Nov. 2021, doi: https://doi.org/10.1016/j.rinp.2021.104902.

(20) D. Homoelle, S. Wielandy, A. L. Gaeta, N. F. Borrelli, and C. G. Smith, "Infrared photosensitivity in silica glasses exposed to femtosecond laser pulses," *Optics Letters*, vol. 24, no. 18, pp. 1311–1311, Sep. 1999, doi: https://doi.org/10.1364/ol.24.001311.

(21) Personal conversations with P. Alcaraz, K. Davalos, B. Davis, K. Gunde, N. Hohner, K. Klosterman, A. Kost, S. McCahon, P. Roumayah, and E. Wilson.

(22) F. El-Diasty, A. Heaney, and T. Erdogan, "Analysis of fiber Bragg gratings by a side-diffraction interference technique," *Applied Optics*, vol. 40, no. 6, p. 890, Feb. 2001, doi: https://doi.org/10.1364/ao.40.000890.

(23) L. Pei, Q. He, J. Wang, J. Zheng, T. Ning, and J. Li, "Complex Refractive Index Profile Measurement for Special Fibers Using Total Variation Method," *Journal of Lightwave Technology*, vol. 41, no. 13, pp. 4097–4102, Jul. 2023, doi: https://doi.org/10.1109/jlt.2022.3224078.